

Efficient MPS representations and quantum circuits from the Fourier modes of classical image data

Bernhard Jobst ^{1,2,3,*} Kevin Shen,^{1,2,3,4,5} Carlos A. Riofrío ³ Elvira Shishenina,³ and Frank Pollmann ^{1,2}

¹*Technical University of Munich, TUM School of Natural Sciences, Physics Department, 85748 Garching, Germany*

²*Munich Center for Quantum Science and Technology (MCQST), Schellingstr. 4, 80799 München, Germany*

³*BMW Group, 80788 München, Germany*

⁴*Leiden University, Niels Bohrweg 1, 2333 CA, Leiden, The Netherlands*

⁵*applied Quantum algorithms (aQa), Leiden University, The Netherlands*

(Dated: December 4, 2023)

Machine learning tasks are an exciting application for quantum computers, as it has been proven that they can learn certain problems more efficiently than classical ones. Applying quantum machine learning algorithms to classical data can have many important applications, as qubits allow for dealing with exponentially more data than classical bits. However, preparing the corresponding quantum states usually requires an exponential number of gates and therefore may ruin any potential quantum speedups. Here, we show that classical data with a sufficiently quickly decaying Fourier spectrum after being mapped to a quantum state can be well-approximated by states with a small Schmidt rank (i.e., matrix product states) and we derive explicit error bounds. These approximated states can, in turn, be prepared on a quantum computer with a linear number of nearest-neighbor two-qubit gates. We confirm our results numerically on a set of 1024×1024 -pixel images taken from the ‘Imagenette’ dataset. Additionally, we consider different variational circuit ansätze and demonstrate numerically that one-dimensional sequential circuits achieve the same compression quality as more powerful ansätze.

I. INTRODUCTION

Quantum computers provide a powerful new platform in the context of machine learning [1, 2], which—in certain instances—can yield a rigorously proven exponential speedup compared to classical machine learning methods [3–7]. Quantum machine learning (QML) algorithms can be applied to quantum data [1, 8–11], where the input data are already given as a quantum state, or to classical data [1, 2, 12–14], where the input data first need to be mapped to a quantum state, which is then prepared as an initial state on the quantum device. This preparation of the initial state is generally exponentially costly [15–17], and thus constitutes a significant bottleneck: even if the subsequent QML algorithm is efficient, the exponential speedup is already lost at the stage of loading the input data [1, 3, 18].

Typical strategies for mapping the classical data to a quantum state leverage the superposition of basis states to encode an exponential amount of data in a linear number of qubits [2, 12, 17]. Thus, intuitively, it is not surprising that the number of gates required to prepare the state scales exponentially in the number of qubits: to fix the exponentially many amplitudes in the quantum state generically exponentially many operations are needed [15]. The scaling can be reduced if it is sufficient to only approximately prepare the state up to a small error. For this, there are several proposals in the literature. Ref. [19] proposes to approximate the state by a truncated Fourier series and prepare it by

loading the lowest-frequency components into a subset of qubits, before extending it to a sparse state on the whole qubit register and running an inverse quantum Fourier transform. If the number of included Fourier modes is fixed, this leads to a circuit with a depth that scales linearly with the number of qubits and a number of CNOT gates that scales quadratically in the number of qubits. However, some long-range two-qubit gates are needed and a priori it is not clear how many Fourier coefficients need to be retained. Another strategy proposed in Refs. [20–23] is to first approximate the data classically by a matrix-product state (MPS), which is argued to be possible due to the observation that states encoding a probability distribution with a bounded derivative have a small entanglement entropy. These MPS can then be prepared with linear-depth quantum circuits on a quantum computer [24–29]. Alternatively, as shown in Ref. [22], one can directly variationally optimize hardware-efficient linear-depth circuits to approximate the target state, which yields circuits that can be faithfully run on current quantum hardware [23]. In both cases, however, it is not clear exactly which bond dimension or circuit depth is needed to accurately capture the target state, and whether or how this has to scale with increasing system size. Other approaches, as proposed in Refs. [30–33], assume a certain structure of the target state to be efficient, i.e., either the number of basis states in the superposition being small [30], all states included in the superposition having a given number of zeros and ones [31, 32] or all weights in the superposition being of a roughly equal magnitude [33]. Additionally, a few of the approaches above use mid-circuit measurements which can be challenging to implement on some hardware realizations, with error rates possibly being an order of

* bernhard.jobst@tum.de

magnitude worse than those of CNOT gates [34–36].

In this work, we focus the discussion on classical image data with sufficiently quickly decaying Fourier coefficients, i.e., those where the coefficients of the Fourier transform as a function of the frequencies k_x and k_y decay faster than $\mathcal{O}(|k_x|^{-1}|k_y|^{-1})$, which we will numerically demonstrate includes most sensible images. However, the results are also applicable to any two-dimensional classical data with Fourier modes decaying in the same way [26, 37–40]. We show that using different mappings from the classical data to a quantum state, the resulting states can be efficiently described by MPS, in the sense that the bond dimension of the MPS does not need to grow with the system size to remain below a certain error threshold. This generalizes the findings of Refs. [20, 21] that real-valued functions with a bounded derivative are well-approximated by MPS, allowing now also for complex-valued functions and diverging derivatives as long as the Fourier coefficients still decay sufficiently fast. We verify our results numerically on 1024×1024 -pixel images taken from the ‘Imagenette’ dataset [41] (a subset of the well-known ImageNet dataset [42]), which contains a variety of images depicting humans, animals and objects, and thus should be reasonably representative of the general features of generic images. The MPS approximation of the quantum state then naturally leads to a linear-depth quantum circuit that only requires a linear number of nearest-neighbor CNOT gates and does not require any mid-circuit measurements [24–29]. Additionally, we try out several different circuit ansätze for variationally compressing images in the Fashion-MNIST dataset [43] (similarly to Ref. [22]), and find that sequential circuits inspired by MPS work just as well as more powerful ansätze with the same number of parameters.

This work is structured as follows: in Sec. II we introduce the different mappings from classical data to quantum states that we consider. In Sec. III, we first present numerical data showing that states encoding classical image data have a small entanglement entropy and are well-approximated by MPS compared to states with randomly sampled amplitudes. Then, we derive explicit bounds on the error of the MPS approximation, depending on the decay of the Fourier modes. Notably, for a fixed bond dimension these bounds do not scale with the systems size. In Sec. IV we compare the numerical results for variationally optimizing different circuit ansätze to approximate states encoding classical image data. Finally, we conclude in Sec. V with a discussion of our results.

II. IMAGE ENCODINGS

Several different strategies for mapping a classical $2^n \times 2^n$ -pixel image to a quantum state have been proposed [17, 44–53]. While we will focus the discussion on images, in principle one could also apply the same mappings to other classical data. The quantum states resulting from the different mappings all share a similar

structure, given by [17]

$$|\psi\rangle = \frac{1}{2^n} \sum_{j=0}^{2^{2n}-1} |c(x_j)\rangle \otimes |j\rangle. \quad (1)$$

Each term in the sum is a tensor product of $|c(x_j)\rangle$ and $|j\rangle$. The state $|c(x_j)\rangle$ is a mapping from the data value x_j of the j th pixel to a quantum state; the number of qubits needed, and whether color or only grayscale images can be taken into account, depend on the details of the chosen encoding. As the corresponding qubits store the information of the pixel values, they are often referred to as *color qubits*. The state $|j\rangle$ lives on $2n$ so-called *address qubits*, and labels each of the 2^{2n} pixels with a binary integer. While the order of this labeling can in principle be chosen arbitrarily, different orders can have an effect on the entanglement entropy of the state. Common choices of the indexing are shown in Fig. 1. Fig. 1a shows a row-by-row indexing of the pixels, as it was e.g. proposed in Ref. [45]; Fig. 1b shows a hierarchical indexing, where the first two qubits label the quadrant of the image in which a pixel lies, the next two qubits label the subquadrant, and so on [44, 45]; and Fig. 1c shows a snake indexing, where every other row is traversed in the reverse direction, which was used in Ref. [22].

In the following, we will present the three most common encodings in some detail. While there exist variants of these that accommodate color images, we will focus on grayscale images.

Amplitude encoding. The simplest strategy for encoding data is *amplitude encoding*. Instead of using another state $|c(x_j)\rangle$ to encode the information of the pixel values, we just use the state amplitudes to encode the information [2, 12, 44]. The state is then given by

$$|\psi\rangle = \frac{1}{\sqrt{\sum_{j=0}^{2^{2n}-1} |x_j|^2}} \sum_{j=0}^{2^{2n}-1} x_j |j\rangle. \quad (2)$$

This way, we only need $2n$ qubits to store the information of 2^{2n} grayscale pixel values, which is an exponential reduction compared to the classical case. However, some information about the contrast of the image, which is present in the classical data, gets lost during this mapping due to the normalization of the quantum state. Before being able to construct such a state on a quantum computer for a given set of pixel values x_j , we first need to decompose the $2n$ -qubit unitary preparing such a state into the native gate set, e.g., CNOT gates and single-qubit gates. While this can be done in principle, the number of gates will generically scale exponentially as $\mathcal{O}(2^{2n})$ [15, 16], and the calculation of the decomposition introduces a classical overhead, which can be computationally costly.

Flexible representation of quantum images. Some of the drawbacks of the amplitude encoding are addressed by the so-called *flexible representation of quantum images (FRQI)* [45, 46]. It uses the general form of

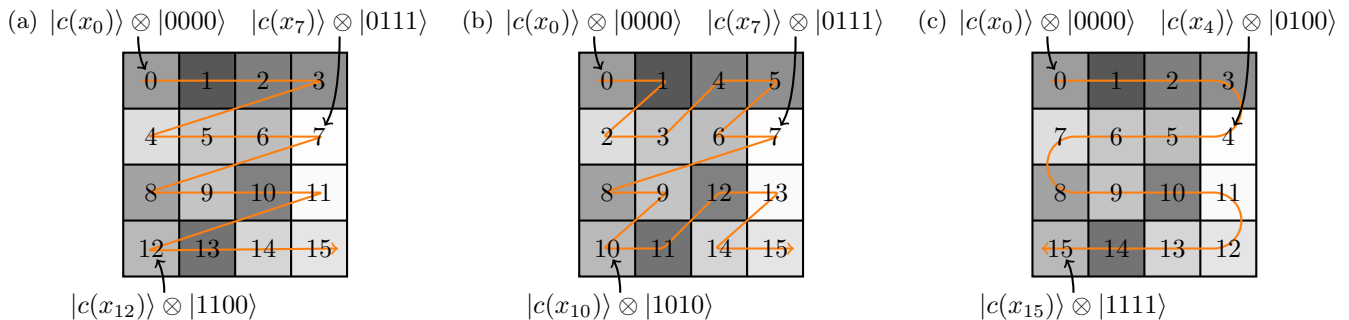


FIG. 1. **Different indexing variants for labeling the pixels in an image during the mapping to a quantum state.** (a) The pixels are labeled row by row from top to bottom and from left to right [45]. This is equivalent to having a separate index for the y - and the x -coordinate and concatenating their binary representation to obtain a single binary integer labeling all pixels. (b) The pixels are labeled in a hierarchical fashion, where the first two bits of the binary integer denote the quadrant of the pixel, the next two bits label the subquadrant, and so on. See also Refs. [44, 45]. (c) The pixels are labeled in a snake pattern that traverses every other row in the opposite direction (used in Ref. [22]).

the state in Eq. (1), and the value x_j of the j th pixel, normalized to lie between 0 and 1, is encoded in the state $|c(x_j)\rangle$ of a single color qubit given by

$$|c(x_j)\rangle = \cos\left(\frac{\pi}{2}x_j\right)|0\rangle + \sin\left(\frac{\pi}{2}x_j\right)|1\rangle. \quad (3)$$

This encodes the 2^{2n} values of a $2^n \times 2^n$ -pixel grayscale image into only $2n + 1$ qubits. (Color images can be treated similarly using several color qubits, see Refs. [50, 51].) Since the state $|c(x_j)\rangle$ is already properly normalized, there is no loss of information after normalizing the final state, in contrast to the amplitude encoding. Additionally, there is a prescription for constructing these states in terms of CNOT gates and single-qubit rotations on a quantum computer, so there is no need for a classical overhead. The state can be constructed exactly using $\mathcal{O}(2^{4n})$ gates [45], or if $2n - 2$ ancilla qubits are present, using $\mathcal{O}(n2^{2n})$ gates [47]. If one does allow for classical preprocessing with $\mathcal{O}(n2^{2n})$ operations, the number of gates can be further reduced to $\mathcal{O}(2^{2n})$ without using ancilla qubits [17]. Using the FRQI, some image processing operations such as pattern detection [54], edge detection [55] and certain color transformations [56] can be implemented efficiently.

Novel enhanced quantum representation of digital images. The pixel values of digital images are usually not given as continuous variables, but rather as discrete 8-bit integers. An encoding based on this is the *novel enhanced quantum representation of digital images (NEQR)* [48]. Given a grayscale $2^n \times 2^n$ -pixel image, where each pixel value x_j can be written as a q -bit binary integer $x_j = x_{0,j}x_{1,j} \dots x_{q-1,j}$ describing one of 2^q different grayscale values, the NEQR maps the image to a quantum state of the form in Eq. (1), with the pixel value x_j being mapped to a q -qubit quantum state given by

$$|c(x_j)\rangle = |x_{0,j}x_{1,j} \dots x_{q-1,j}\rangle. \quad (4)$$

This encodes the 2^{2n} pixel values of a grayscale image into $2n + q$ qubits. (Color images can also be represented

in this framework using more color qubits, see Refs. [52, 53].) The state can be prepared exactly on a quantum computer using $\mathcal{O}(qn2^{2n})$ CNOT and single-qubit gates if one utilizes $2n - 2$ ancilla qubits [48]. If one allows for $\mathcal{O}(qn2^{2n})$ operations of classical preprocessing, the state can be prepared using $\mathcal{O}(q2^{2n})$ gates without using any ancilla qubits [17]. Compared to the FRQI, more color transformations can be implemented efficiently [48], and algorithms for feature extraction and image scaling have been proposed [57, 58].

For all three encodings, the asymptotic scaling of the number of gates needed to prepare the state is exponential in the number of qubits. The exponential cost for preparing the state exactly seems to be unavoidable in a general setting, since we need to load exponentially many pixel values into the quantum state.

III. IMAGE COMPRESSION WITH MPS

For machine learning tasks, it is usually not necessary to prepare the exact quantum state representing the image, a good approximation of the state is sufficient. The idea is that as long as we are close enough to the target state, we can view the input state as the exact training data with some noise added, and the classifier should still be able to recognize relevant features and assign the correct label. In fact, in classical machine learning it was observed that adding random noise to the training data can act as a kind of regularization and actually improve the generalization of the classifier [60–62]. Similarly, for QML algorithms applied to quantum data, Ref. [10] found that adding perturbations to quantum states during training helps the classifier to learn to distinguish different quantum phases of matter, while for QML algorithms applied to classical data, Ref. [22] found numerically that the classifier is still able to learn from the quantum states in the training set if they are only prepared approximately.

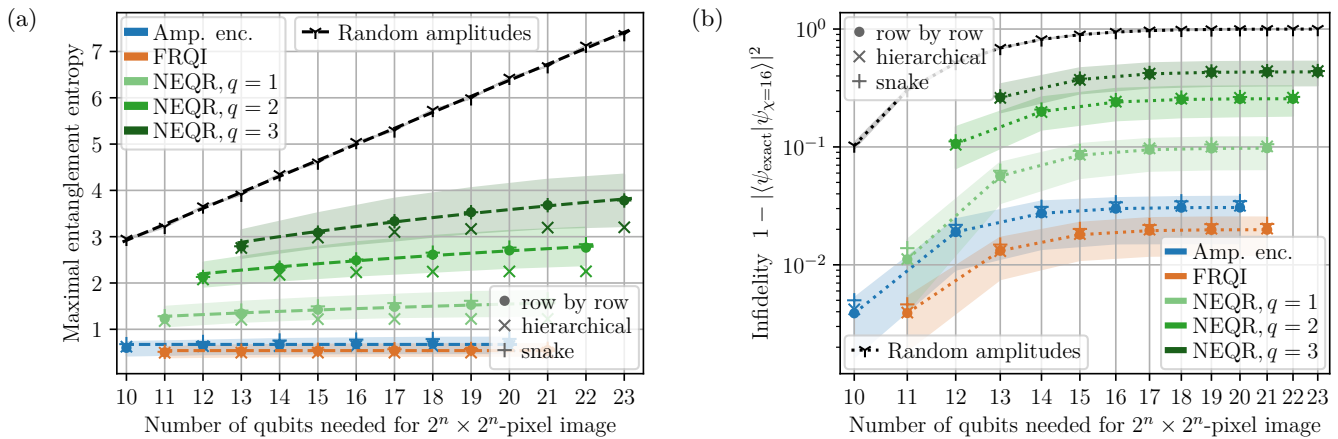


FIG. 2. **Scaling of the entanglement entropy and the approximation error with increasing image size.** The quantum states are obtained from encoding the 174 highest-resolution images of the ‘Imagenette’ dataset [41] for different image sizes. (a) The plot shows the scaling of the maximal entanglement entropy over any bipartition of the state into two contiguous halves. Blue markers show the results using amplitude encoding, orange markers the results using the FRQI, and the different shades of green show the results using the NEQR with 1–3 color qubits. The marker shapes—dots, crosses and pluses—indicate the different indexing variants—respectively, row-by-row indexing, hierarchical indexing and snake indexing (see also Fig. 1). The shaded areas show the 25th–75th percentiles for the different encodings using row-by-row indexing. The dashed blue and orange lines show the average value of the entanglement that is approached with increasing image size, the green dashed lines show logarithmic fits. For reference, we also show the average half-chain entanglement entropy for 100 states whose amplitudes were drawn from a normal distribution before normalization as black three-pointed stars, the black shaded area shows the 25th–75th percentiles. The black dashed line is a linear fit to the data, showing the generic growth of entanglement with system size [59]. (b) The plot shows the state infidelity between the exact encoded state and its bond dimension $\chi = 16$ approximation of the state. The colors and marker shapes denote the same encodings as before.

If we relax the constraint of preparing the target state exactly and allow for a small approximation error, we can overcome the exponential scaling of the number of gates needed to prepare the state. For small images, Ref. [22] found that matrix-product states (MPS) with a small bond dimension and shallow quantum circuits, i.e., circuits with a number of gates scaling linearly in the number of qubits, suffice to approximate the corresponding quantum states well enough, so that a classifier trained on these compressed states is still able to learn the classification task. The question remains, however, whether this observation also scales to much larger images.

A. Numerical results

To test the scaling of compressing images into quantum states, we consider images in the ‘Imagenette’ dataset [41], which is a subset of the well-known large-scale ImageNet dataset [42] and contains a variety of photographs of humans, animals and objects in front of different backgrounds. Thus, this dataset should capture a wide variety of features that commonly occur in natural images, and thus can be expected to be reasonably representative for drawing general conclusions about the properties of generic images. In particular, we select the 174 images in the dataset with a resolution higher than 1024×1024 pixels, as we are interested in the scaling towards large image sizes. To achieve a uniformly sized

test set, we take the largest square section of the images and resize them to all have the fixed size of 1024×1024 pixels using bilinear interpolation. We map the images to quantum states according to the encodings discussed in Sec. II, and we consider different image resolutions by repeatedly halving the image size by only retaining every other pixel in the smaller image.

First, we look at the entanglement entropy of these states, as low-entangled states are usually well-approximated by MPS [63–67]. A good MPS approximation also implies a polynomial-depth circuit, as an n -qubit MPS with a fixed bond dimension χ can be prepared using $\mathcal{O}(\chi^2 n)$ gates [24–29].

Fig. 2a shows the maximal entanglement entropy over all bipartitions of the state into two contiguous halves, averaged over all images in the dataset. The different colors denote the different encodings, i.e., blue shows the data for amplitude encoding, orange the data for the FRQI and the different shades of green the data for the NEQR with 1–3 color qubits. The marker shapes denote the different ways the pixel are indexed (see Fig. 1); dots show the data for row-by-row indexing, crosses the data for hierarchical indexing and pluses the data for snake indexing. The shaded areas show the 25th–75th percentiles for the different image encodings using the row-by-row indexing; we omit the shaded areas for the data points corresponding to the other indexing variants for visual clarity, the results would look similar. As a reference value, we also plot the half-chain entanglement

entropy of states with amplitudes that are sampled randomly from a normal distribution with zero mean and a variance of one before normalization. The average of 100 realizations is marked by black three-pointed stars, the 25th–75th percentiles are shaded in black. The black dashed line shows a linear fit to the data, illustrating the generic case where the entanglement entropy of quantum states grows linearly with the subsystem size [59]. Conversely, we see that states using amplitude encoding or the FRQI to represent images, independent of the type of indexing used, display a saturation of the entanglement entropy at rather small values with growing image size. The limiting value of the entanglement entropy is roughly reached for image sizes 64×64 and above, the averages of these data points are shown as blue and orange dashed lines. In comparison, the entanglement entropy of states using the NEQR is larger, but still smaller than the generic case, and for the system sizes at hand it is not quite clear whether the growth of the entanglement entropy will eventually saturate. The green dashed lines show the results of fitting a growth logarithmic in the number of qubits to the data.

The saturation of the entanglement entropy at comparably small values for states using amplitude encoding or the FRQI suggests that these states can be well-approximated by MPS with a small bond dimension, while the approximation should be significantly worse for states using the NEQR. Fig. 2b shows the average infidelity of the exact encoded states and an MPS approximation with bond dimension $\chi = 16$. The MPS approximation is obtained by performing subsequent singular value decompositions (SVDs) of the original state and only keeping the χ dominant singular values [68]. As before, the different colors indicate the different image encodings, and the marker shapes denote the different indexing styles. The shaded areas show the 25th–75th percentiles for different encodings using the row-by-row indexing. For reference, we again show the results for states with randomly sampled amplitudes as black three-pointed stars. We see that the average infidelity of states using amplitude encoding and the FRQI is below that of the NEQR, confirming our expectation. For all three encodings, the average infidelity is far below that of the random states, which cannot be effectively approximated by an MPS with bond dimension $\chi = 16$. For states using amplitude encoding and the FRQI, the infidelity seems to saturate with increasing system size at some value, just like the entanglement entropy; for the NEQR, it is again not quite clear whether the error saturates or grows very slowly. The observation that (for certain encodings) the infidelity does not grow asymptotically has significant consequences for the asymptotic scaling of the state preparation. Since the MPS approximation can be prepared using $\mathcal{O}(\chi^2 n)$ gates, and we do not need to increase χ with increasing system size, the preparation will only scale linearly in the system size.

An example for the quality of the compression is shown in Fig. 3. The uncompressed image, shown in Fig. 3a, is

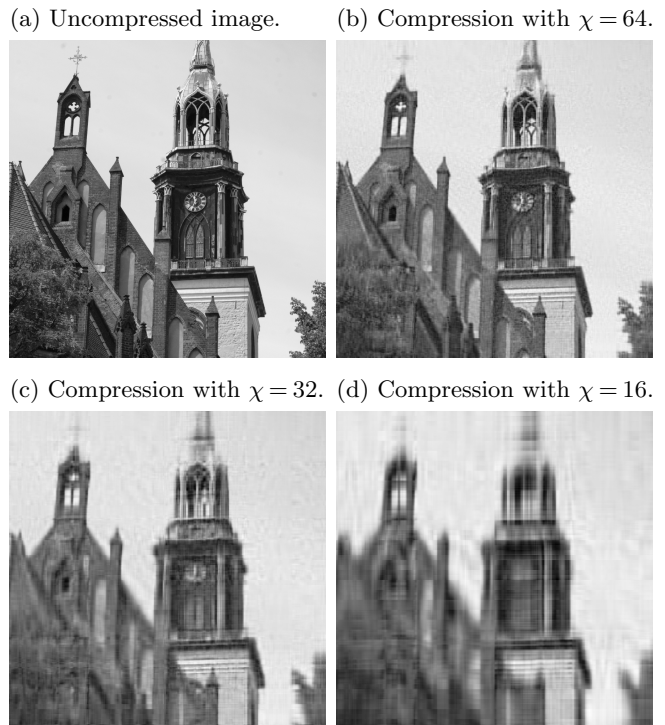


FIG. 3. Comparing an (a) uncompressed image to its MPS approximations with different bond dimensions (b) $\chi = 64$, (c) $\chi = 32$ and (d) $\chi = 16$. (a) The original image with 1024×1024 pixels is obtained from resizing the raw data of the camera, without using any image compression. (b) Compressing the image with a bond dimension $\chi = 64$ yields an infidelity of 0.006, (c) a bond dimension $\chi = 32$ yields an infidelity of 0.011, and (d) a bond dimension $\chi = 16$ yields an infidelity of 0.017.

obtained from the raw data of a digital camera, and then resized to 1024×1024 pixels. The compressed images are obtained by mapping the original image to a quantum state using amplitude encoding with row-by-row indexing, and constructing an MPS with bond dimension χ by performing subsequent SVDs and keeping only the dominant χ singular values. The approximation with $\chi = 16$ is shown in Fig. 3d; in Fig. 2b we showed the infidelities of MPS approximations with bond dimension $\chi = 16$ for states using amplitude encoding, so this image is representative of the compression quality that can be achieved in these cases. For the image shown, the infidelity of the original state and the MPS approximation is 0.017. Increasing the bond dimension to $\chi = 32$ and $\chi = 64$ leads to a better approximation, as shown in Figs. 3c and 3b, and yields the smaller infidelities of 0.011 and 0.006, respectively.

B. Bounds on the approximation error

In this section we derive error bounds for the MPS approximation of quantum states that encode image data.

For this we focus on a specific subset of images, i.e., those with Fourier coefficients that decay strictly faster than $\mathcal{O}(|p|^{-1}|q|^{-1})$ as a function of the Fourier frequencies p and q in x - and y -direction. This includes most typical images, where the high-frequency components are small, as high-frequency changes in the pixel values are usually perceived as noise—this assumption also underlies classical image compression methods like the JPEG compression algorithm. In practice, we can look at the same 174 images from the ‘Imagenette’ dataset [41] we used before and calculate the mean absolute value of the Fourier coefficients; the results are shown in Fig. 4. The color plot shows the full spectrum, where most of the weight is concentrated in the bright white spot in the center and the two lines where either the frequency in the x - or the y -direction (labeled by p and q) are zero. Outside this region, the weight of the coefficients decreases quickly with increasing frequency. The plot below in the figure shows cuts through the upper color plot along the two white lines, i.e., for either of the two frequencies being zero. In both cases the weight of the Fourier coefficients decays approximately algebraically, indicated by the dashed lines which show algebraic fits to the data, and the decay is faster than $\mathcal{O}(1/p)$ or $\mathcal{O}(1/q)$, respectively. The deviation for large frequencies can be understood as a finite-size effect, see the discussion in the following and the derivation in App. B.

To derive the error bounds, we first focus on states using amplitude encoding with row-by-row indexing, i.e., for data given as a $2^n \times 2^n$ matrix f_{ab} with $a, b \in \{0, 1, \dots, 2^n - 1\}$, the quantum state is of the form

$$|\psi\rangle = \frac{1}{\sqrt{\sum_{a,b=0}^{2^n-1} |f_{ab}|^2}} \sum_{a,b=0}^{2^n-1} f_{ab} |b\rangle |a\rangle. \quad (5)$$

The strategy is then to relate the Fourier coefficients of an $2^n \times 2^n$ -pixel image to the Fourier coefficients of an ‘infinitely high-resolution’ image. Then, we explain how to construct an MPS from a truncated Fourier series, before showing that a truncated Fourier series is a good approximation if the Fourier coefficients decay fast enough. Finally, we discuss how to extend the derived error bounds to the other indexing and encoding variants.

Fourier representation. As the goal is to understand the limiting behavior of the quantum states as the number of qubits tends to infinity, we need to specify the limit that the image data approach as the system size increases. We can describe this limiting value by a function

$$F : [0, 1)^2 \subset \mathbb{R}^2 \rightarrow \mathbb{C}, \quad (x, y) \mapsto F(x, y) \quad (6)$$

with continuous inputs x and y defined on the unit square. In principle, this could describe any form of data, but in terms of images, one can restrict to functions with real outputs and think of them as the light intensity distribution of a subject convolved with the point spread function of an imaging system, e.g., one could think of

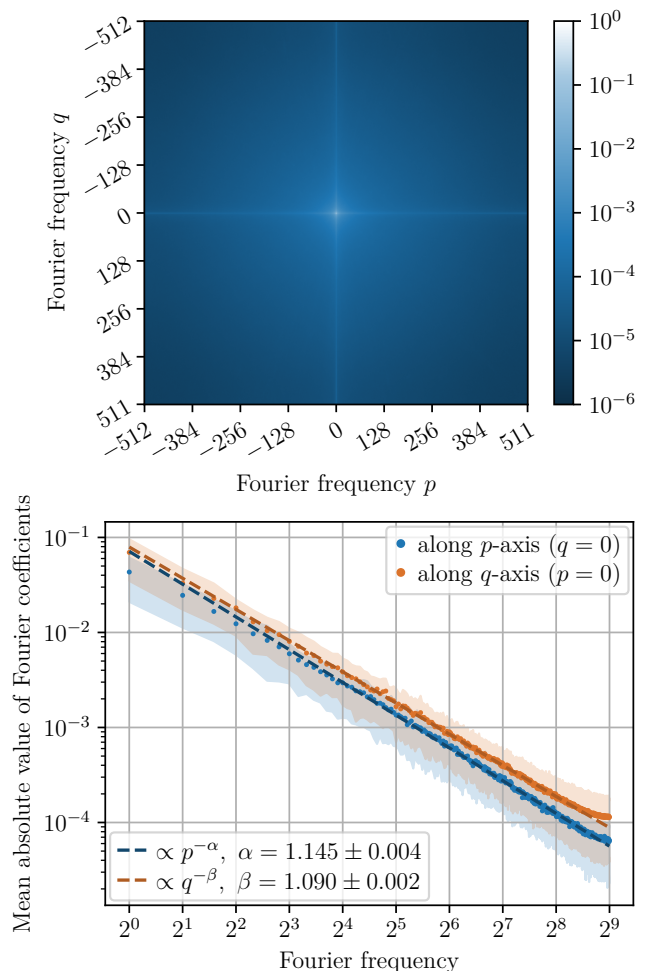


FIG. 4. **Average decay of the Fourier coefficients of 1024×1024 -pixel images.** The color plot shows the average absolute values of the 174 highest-resolution images of the ‘Imagenette’ dataset [41]. Most of the weight is concentrated at the bright white spot in the center, and the two axes corresponding to zero-frequency modes in either direction. The plot below shows the decay of the average absolute value of the Fourier coefficients along the zero-frequency modes—along the p -axis where $q = 0$ in blue and along the q -axis where $p = 0$ in orange. The shaded areas show the 25th–75th percentiles. The decay is almost algebraic, as shown by the algebraic fits to the data that are plotted as dashed lines. The deviation from the algebraic decay for larger frequencies is due to finite-size effects, see Eq. (B19) in the Appendix.

a grayscale image taken by a digital camera with ‘infinitely high resolution’. From this function with continuous variables, we obtain the $2^n \times 2^n$ -pixel image f_{ab} by evaluating it at discrete points $(x, y) = (\frac{a}{2^n}, \frac{b}{2^n})$, with $a, b \in \{0, 1, \dots, 2^n - 1\}$. To differentiate between the function with continuous inputs describing the limit of infinite pixels and the $2^n \times 2^n$ -pixel image with discrete indices, we denote the former by an uppercase F and the latter by a lowercase f (and we will also stick to this convention for their Fourier transforms \hat{F} and \hat{f} in the

following). We can write the Fourier series of the function F in Eq. (6) as

$$F(x, y) = \sum_{k, \ell=-\infty}^{\infty} \hat{F}(k, \ell) e^{i2\pi kx} e^{i2\pi \ell y} \quad (7)$$

$$\hat{F}(k, \ell) = \int_0^1 dx \int_0^1 dy F(x, y) e^{-i2\pi kx} e^{-i2\pi \ell y}.$$

and relate it to the discrete Fourier transform (DFT) of the pixelated image as

$$f_{ab} = \sum_{p, q=-2^{n/2}}^{2^{n/2}-1} \hat{f}_{pq} e^{i2\pi pa/2^n} e^{i2\pi qb/2^n} \quad (8)$$

$$\parallel$$

$$F\left(\frac{a}{2^n}, \frac{b}{2^n}\right) = \sum_{k, \ell=-\infty}^{\infty} \hat{F}(k, \ell) e^{i2\pi ka/2^n} e^{i2\pi \ell b/2^n},$$

where $\hat{F}(k, \ell)$ are the coefficients of the Fourier series of the function $F(x, y)$ with continuous arguments as in Eq. (7) and \hat{f}_{pq} are the coefficients obtained from the DFT of the pixelated image f_{ab} . Since the phase factor $e^{i2\pi ka/2^n}$ is invariant under shifts $k \rightarrow k + j2^n$ with $j \in \mathbb{Z}$ and the DFT is unique, we can identify

$$\hat{f}_{pq} = \sum_{i, j \in \mathbb{Z}} \hat{F}(p + i2^n, q + j2^n). \quad (9)$$

This allows to relate the Fourier coefficients \hat{f}_{pq} of the $2^n \times 2^n$ -pixel image to those of the sampled function $\hat{F}(k, \ell)$, and allows us to study what happens as the number of pixels is increased.

Consider, for example, a function F with some cutoff Λ in the Fourier spectrum, i.e., all Fourier coefficients $\hat{F}(k, \ell)$ are zero if either $|k| > \Lambda$ or $|\ell| > \Lambda$. Then for large enough images, where $2^n > 2\Lambda$, we see from Eq. (9) that the Fourier coefficients remain unchanged when increasing n because shifting the Fourier frequencies by 2^n always takes them outside of the cutoff. The image can then be written as

$$f_{ab} = \sum_{p, q=-\Lambda}^{\Lambda} \hat{F}(p, q) e^{i2\pi pa/2^n} e^{i2\pi qb/2^n}, \quad (10)$$

i.e., as a sum of a finite number of Fourier modes, and now neither the value of the Fourier coefficients nor the number of Fourier modes in the sum depend on n .

MPS from Fourier modes. It turns out that matrices containing only a few Fourier modes, such as for the case above, can be written efficiently as an MPS. An MPS for n qubits has the form [69, 70]

$$|\psi\rangle = \sum_{\{\sigma_j\}_{j=0}^{n-1}} A^{[0]\sigma_0} A^{[1]\sigma_1} \dots A^{[n-1]\sigma_{n-1}} \times |\sigma_0 \sigma_1 \dots \sigma_{n-1}\rangle, \quad (11)$$

where for each qubit j there are two $\chi_j \times \chi_{j+1}$ matrices $A^{[j]\uparrow}$ and $A^{[j]\downarrow}$, and the probability amplitude for a given

basis state is obtained by performing the matrix multiplication of the corresponding matrices. For the matrix multiplication to yield a number, the matrix dimensions χ_0 and χ_n must be one. The maximal matrix dimension $\chi = \max_j \chi_j$ is often referred to as the bond dimension of the MPS, and it controls the amount of entanglement contained in the state. Any state can be written as an MPS, however, generically the bond dimension will need to increase exponentially with the system size n —in certain cases, the bond dimension does not scale with the system size and the 2^n amplitudes of the quantum state can be expressed using only $\mathcal{O}(\chi^2 n)$ parameters.

In one dimension, a sum of χ Fourier modes can be written as an MPS with bond dimension χ [71–75]. This can be seen by first considering an n -qubit state with coefficients given by a single Fourier mode:

$$|\psi\rangle = \frac{1}{\sqrt{2^n}} \sum_{a=0}^{2^n-1} e^{i2\pi ka/2^n} |a\rangle. \quad (12)$$

We can express the summation index a as an n -bit binary, $a = \sum_{j=0}^{n-1} 2^{n-1-j} \sigma_j$ with $\sigma_j \in \{0, 1\}$, and find

$$|\psi\rangle = \frac{1}{\sqrt{2^n}} \sum_{\{\sigma_j\}_{j=0}^{n-1}} e^{i2\pi k \sum_{j=0}^{n-1} 2^{n-1-j} \sigma_j / 2^n} |\sigma_0 \sigma_1 \dots \sigma_{n-1}\rangle \quad (13)$$

$$= \bigotimes_{j=0}^{n-1} \left(\frac{1}{\sqrt{2}} \sum_{\sigma_j=0}^1 e^{i2\pi k \sigma_j / 2^{j+1}} |\sigma_j\rangle \right),$$

i.e., a single Fourier mode corresponds to a product state. Hence, a sum of χ Fourier modes can be written as a bond dimension χ MPS.

In two dimensions, a sum of Fourier modes given by a $\chi \times \chi$ matrix of Fourier coefficients can be similarly written as a bond dimension χ MPS—the qubits corresponding to the x - and y -coordinates each contain plane waves with χ different frequencies, and the two qubit registers are connected by the $\chi \times \chi$ matrix of Fourier coefficients. The detailed derivation can be found in App. A. See Fig. 5a for a graphical representation.

Consider the previous example of a Fourier series with a cutoff Λ in Eq. (10); there is only a $(2\Lambda + 1) \times (2\Lambda + 1)$ matrix of Fourier modes that contributes to the Fourier series, so we can express the state as an MPS with bond dimension $\chi = 2\Lambda + 1$. Since the number of terms in the Fourier series does not increase with increasing pixel number, the bond dimension of the MPS will be constant as we increase the number of pixels.

Error bounds for decaying Fourier coefficients. Generically, the Fourier spectrum of relevant images will not have a cutoff. Rather, the magnitude of the Fourier coefficients decays with increasing frequency (see also Fig. 4). Here, we consider the approximation error when approximating an image by retaining only Fourier modes up to some cutoff—the resulting state can then be described by an MPS with fixed bond dimension, even if the number of pixels goes to infinity.

In the following, to simplify the notation, we introduce three index sets. First, the set of all frequency pairs contributing to the Fourier transform of a $2^n \times 2^n$ -pixel image, $I_{\text{all}} = \{-2^n/2, -2^n/2 + 1, \dots, 2^n/2 - 1\}^2$, secondly, the set of all frequency pairs contained in the approximation, $I_{\text{appr}} = \{-\Lambda, -\Lambda + 1, \dots, \Lambda\}^2$, and finally, the set of frequency pairs discarded in the approximation, $I_{\text{disc}} = I_{\text{all}} \setminus I_{\text{appr}}$. Using this, the pixel values f_{ab} can be expressed in terms of their Fourier modes as

$$f_{ab} = \sum_{(p,q) \in I_{\text{all}}} \hat{f}_{pq} e^{i2\pi pa/2^n} e^{i2\pi qb/2^n} = 2^n (U \hat{f} U^T)_{ab}, \quad (14)$$

viewing \hat{f}_{pq} as a matrix and introducing the unitary matrix $U_{ap} = \frac{1}{\sqrt{2^n}} e^{i2\pi pa/2^n}$. Note the factor 2^n in Eq. (14), which appears due to the convention of the Fourier transform used in Eq. (8). In the same way, we can write the pixel values g_{ab} obtained from approximating f_{ab} by truncating the Fourier spectrum; this gives

$$g_{ab} = \sum_{(p,q) \in I_{\text{appr}}} \hat{g}_{pq} e^{i2\pi pa/2^n} e^{i2\pi qb/2^n} = 2^n (U \hat{g} U^T)_{ab}, \quad (15)$$

where \hat{g} is the matrix of the truncated Fourier coefficients, i.e., for $|p| \leq \Lambda$ and $|q| \leq \Lambda$ we have $\hat{g}_{pq} = \hat{f}_{pq}$ but if either $|p| > \Lambda$ or $|q| > \Lambda$ then $\hat{g}_{pq} = 0$.

The quantum state corresponding to the exact image is

$$|f\rangle = \frac{1}{\|f\|_F} \sum_{a,b=0}^{2^n-1} f_{ab} |b\rangle |a\rangle, \quad (16)$$

where $\|f\|_F = \sqrt{\sum_{a,b=0}^{2^n-1} |f_{ab}|^2}$ denotes the Frobenius norm of the matrix of pixel values, and the quantum state corresponding to the approximation of the image is

$$|g\rangle = \frac{1}{\|g\|_F} \sum_{a,b=0}^{2^n-1} g_{ab} |b\rangle |a\rangle. \quad (17)$$

The error of the approximation is given by the norm of the difference of the two states, $\| |f\rangle - |g\rangle \|_2$, using the usual 2-norm $\|\psi\|_2 = \sqrt{\langle \psi | \psi \rangle}$.¹ This expression can then be bounded by

$$\| |f\rangle - |g\rangle \|_2 \leq \frac{2\|f - g\|_F}{\|g\|_F}, \quad (18)$$

¹ Previously, we have used the fidelity $\mathcal{F} = \langle f | g \rangle^2$ (or the related infidelity $1 - \mathcal{F}$) as a measure of closeness between two states $|f\rangle$ and $|g\rangle$. The two quantities can be related by rewriting the norm of the difference of the two states as

$$\| |f\rangle - |g\rangle \|_2^2 = (\langle f | - \langle g |) (|f\rangle - |g\rangle) = 2(1 - \text{Re} \langle f | g \rangle).$$

By allowing a change in the global phase of $|g\rangle$, we can make the overlap $\langle f | g \rangle$ purely real, and can relate the two quantities as

$$\| |f\rangle - |g\rangle \|_2 = \sqrt{2(1 - \sqrt{\mathcal{F}})} \quad \text{or} \quad \mathcal{F} = \left(1 - \frac{1}{2} \| |f\rangle - |g\rangle \|_2^2\right)^2.$$

which is proved in App. B. Expressing this in terms of the Fourier coefficients gives

$$\begin{aligned} \| |f\rangle - |g\rangle \|_2 &\leq \frac{2\|f - g\|_F}{\|g\|_F} \\ &= \frac{2 \cdot 2^n \|U(\hat{f} - \hat{g})U^T\|_F}{2^n \|U\hat{g}U^T\|_F} = \frac{2\|\hat{f} - \hat{g}\|_F}{\|\hat{g}\|_F}, \end{aligned} \quad (19)$$

where we have used that the Frobenius norm is invariant under multiplication by a unitary matrix. Thus, to get the approximation error we just need to bound the norm of the difference of the Fourier coefficients. Since \hat{g} has the same values as \hat{f} inside the cutoff, but is zero outside the cutoff, the norm of the difference amounts to calculating the weight of the discarded Fourier coefficients, i.e.,

$$\|\hat{f} - \hat{g}\|_2 = \sqrt{\sum_{(p,q) \in I_{\text{disc}}} |\hat{f}_{pq}|^2}. \quad (20)$$

This sum converges if the Fourier coefficients decay fast enough.

In particular, if we assume that the Fourier coefficients $\hat{F}(k, \ell)$ of the function $F(x, y)$ decay exponentially as

$$|\hat{F}(k, \ell)| \leq C e^{-\alpha|k|} e^{-\beta|\ell|}, \quad (21)$$

with some constants $C, \alpha, \beta > 0$, we can bound the absolute value of the Fourier coefficients \hat{f}_{pq} of the $2^n \times 2^n$ -pixel image via Eq. (9) and obtain a bound for the approximation error $\epsilon = \| |f\rangle - |g\rangle \|_2$ as

$$\begin{aligned} \epsilon &\leq \frac{2C}{\|\hat{g}\|_F} \left(\frac{\coth(\beta)}{\sinh(\alpha)} e^{-\alpha\chi} + \frac{\coth(\alpha)}{\sinh(\beta)} e^{-\beta\chi} \right. \\ &\quad \left. + \frac{e^{-(\alpha+\beta)\chi}}{\sinh(\alpha)\sinh(\beta)} \right)^{\frac{1}{2}} + \mathcal{O}\left(2^n e^{-\alpha 2^n}, 2^n e^{-\beta 2^n}\right), \end{aligned} \quad (22)$$

see App. B for the detailed calculation. Importantly, this bound does not increase with an increasing number of pixels, and corrections to this bound decay exponentially with the image size. Note that the factor $1/\|\hat{g}\|_F$ does not change the asymptotic scaling, as it is dominated by the $(2\Lambda + 1) \times (2\Lambda + 1)$ smallest-frequency Fourier modes $\hat{F}(k, \ell)$. The corrections due to a finite size of the $2^n \times 2^n$ -pixel image are exponentially small in 2^n , see Eq. (B5). Since $\|\hat{g}\|_F$ cannot become arbitrarily small,² its inverse cannot induce a factor in the error bound that diverges asymptotically, and thus does not change the scaling. The approximation error decreases exponentially as $\mathcal{O}(e^{-\min(\alpha, \beta)\chi/2})$ with the bond dimension χ , or conversely, if we want to describe the image with a fixed

² This is the case unless we consider edge cases where all Fourier coefficients $\hat{F}(k, \ell)$ with $|k|, |\ell| \leq \Lambda$ are exactly zero, in which case one should rather consider a frequency range with nonzero Fourier coefficients for the approximation, e.g., $\Lambda < |k|, |\ell| \leq 2\Lambda$.

error ϵ as the image size is increased, the bond dimension scales as $\mathcal{O}(\log(1/\epsilon))$, which is independent of n .

The more relevant case for images is when the Fourier coefficients $\hat{F}(k, \ell)$ decay algebraically as

$$|\hat{F}(k, \ell)| \leq C \frac{1}{(|k| + 1)^\alpha} \frac{1}{(|\ell| + 1)^\beta}, \quad (23)$$

with some constants $C > 0$ and $\alpha, \beta > 1$. We need $\alpha, \beta > 1$ so that the Fourier series converges absolutely and we can use Eq. (9) to bound the absolute values of the Fourier coefficients \hat{f}_{pq} of the $2^n \times 2^n$ -pixel image. In this case, we can obtain an asymptotic bound for the approximation error as

$$\epsilon \leq \sqrt{\mathcal{O}(\Lambda^{1-2\alpha}) + \mathcal{O}(\Lambda^{1-2\beta})} + \mathcal{O}((2^n)^{1-2\alpha}, (2^n)^{1-2\beta}). \quad (24)$$

The derivation and a more detailed expression for the bound are given in App. B. This means that to achieve an approximation error ϵ for a $2^n \times 2^n$ -pixel image the bond dimension needs to scale as $\mathcal{O}\left((1/\epsilon)^{1/(\min(\alpha, \beta) - \frac{1}{2})}\right)$, which—notably—is independent of n .

Note that the usual definition of an efficient approximation by MPS means that the bond dimensions only need to grow polynomially with the system size to keep the approximation error constant [63, 64]. Here, the result is even stronger than that, as the bond dimension does not scale asymptotically with the system size at all.

Extensions of the results. The results presented here were for states using amplitude encoding with the row-by-row indexing. However, they can easily be extended to the hierarchical and snake indexing, as well as to the FRQI. We will also discuss why the NEQR generically does not fit into this framework.

First, we consider the hierarchical indexing. For hierarchical indexing, the first two qubits label the quadrant of the image in which the pixel can be found. For row-by-row indexing, these two qubits correspond to the most significant bit of the x - and y -coordinates. The next two qubits for hierarchical indexing label the subquadrant in which the pixel lies. This corresponds to the next-most significant bits of the x - and y -coordinates of the row-by-row indexing. Thus, we can obtain the state using hierarchical indexing from the state using row-by-row indexing by alternately interleaving qubits corresponding to the x - and y -coordinate, ordered from most significant to least significant bit. Fig. 5a shows the MPS of the state using row-by-row indexing, and Fig. 5b shows the result of swapping the qubits into an alternating pattern to construct the state using hierarchical indexing. Thus, from the results of the previous section we can conclude that also states using hierarchical indexing can be approximated by MPS with a bond dimension that does not scale with the system size. Note that while this construction of the MPS increases the bond dimension from χ to χ^2 , from the numerical results in Fig. 2b we see that an MPS-approximation with bond dimension χ of a

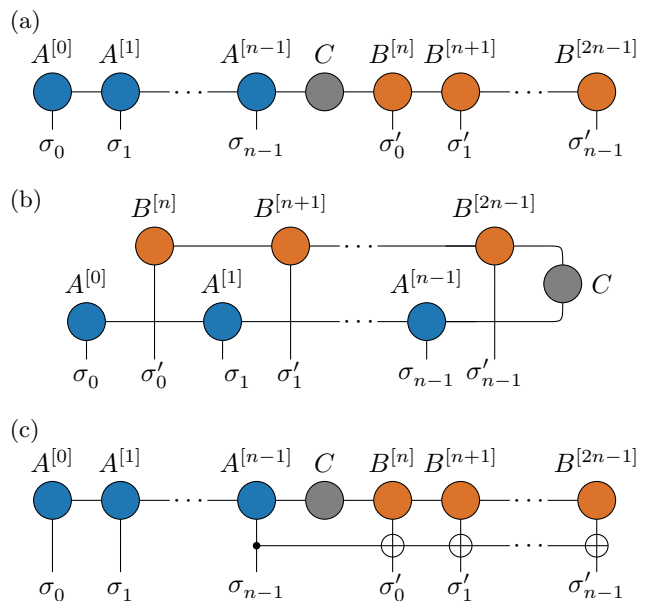


FIG. 5. MPS representation of amplitude encoding state using (a) row-by-row, (b) hierarchical and (c) snake indexing. Consider a $2n$ -qubit amplitude encoding state $|\psi\rangle \propto \sum_{a,b} f_{ab}|b\rangle|a\rangle$, whose amplitudes f_{ab} can be written as a sum of $\chi \times \chi$ Fourier modes. The first n qubits corresponding to the index b (the y -coordinate) are labeled σ_j , the remaining n qubits corresponding to the index a (the x -coordinate) are labeled σ'_j . The $A^{[j]}$ tensors correspond to the plane waves on the y -register, the $B^{[j]}$ tensors correspond to the plane waves on the x -register, and C contains the Fourier modes—see also App. A for the notation. (a) The MPS representation of the state using row-by-row indexing has bond dimension χ . (b) By reordering the qubits we obtain the hierarchical indexing. Note that all the MPS tensors $B^{[j]}$ are diagonal (see App. A), and so their order can be exchanged. This gives an MPS with bond dimension χ^2 . (c) The snake indexing can be obtained by applying a CNOT gate with one control and several target qubits. This gate can be written as a matrix product operator with bond dimension equal to two, so the bond dimension of the resulting MPS is 2χ .

state using hierarchical indexing is about as good or better than an MPS-approximation with bond dimension χ of a state using row-by-row indexing.

Next, we consider snake indexing. To obtain snake indexing from the row-by-row indexing, we need to mirror the x -coordinate for every other y -coordinate. Mirroring the x -coordinate can be done by applying Pauli- X gates on the whole register corresponding to the x -coordinate. Doing this only for every other row means making these Pauli- X gates conditional on the least significant bit of the y -coordinate. This means we need to apply a CNOT gate with one control and several target qubits, which is shown graphically in Fig. 5c. Such a gate can be written as a matrix product operator (MPO), where the two-dimensional virtual index carries the information of whether the control qubit was in the state $|0\rangle$ or $|1\rangle$, and depending on that the tensor connecting the two physical

indices either forms an identity matrix or a Pauli- X gate. Such an MPO can change the bond dimension of the MPS at most by a factor of two. Thus, also states using the snake indexing can be expressed as states where the bond dimension does not need to grow with increasing system size.³

We can also extend the MPS approximability to the FRQI, by writing out the state as

$$\begin{aligned} |\psi\rangle &= \frac{1}{2^n} \sum_{a,b=0}^{2^n-1} |c(f_{ab})\rangle \otimes |b\rangle |a\rangle \\ &= \sum_{a,b=0}^{2^n-1} \frac{1}{2^n} \cos\left(\frac{\pi}{2} f_{ab}\right) |0\rangle \otimes |b\rangle |a\rangle \\ &\quad + \sum_{a,b=0}^{2^n-1} \frac{1}{2^n} \sin\left(\frac{\pi}{2} f_{ab}\right) |1\rangle \otimes |b\rangle |a\rangle. \end{aligned} \quad (25)$$

This can be viewed as the sum of two states using amplitude encoding, one encoding $\frac{1}{2^n} \cos(\frac{\pi}{2} f_{ab})$ and the other one encoding $\frac{1}{2^n} \sin(\frac{\pi}{2} f_{ab})$. Since the decay of the Fourier coefficients can be related to the smoothness of the function [77], and the sine and cosine functions are analytic, the newly encoded functions are also smooth and should have similarly decaying Fourier coefficients.⁴ This is also observed numerically in Fig. 2b, where the approximation error of the states using the FRQI is even smaller than that of those using amplitude encoding.

While it seems like this trick can also be applied to the NEQR, now with 2^q copies of amplitude encoding states instead of just two, this is not quite the case. For simplicity, let us assume $q = 1$; then, the NEQR would correspond to two copies of amplitude encoding states.

³ One could have also considered an ordering of the pixels as given by the Gray code, where the binary integers labeling the x - and y -coordinate are ordered such that subsequent integers differ only by a single bit. A circuit implementing such a transform is given by a staircase of CNOT gates [76], so one can connect the row-by-row indexing to the Gray-code indexing (similarly to how the snake indexing can be connected to the row-by-row indexing) by applying the appropriate unitary gate: in this case, a staircase of CNOT gates on both the x - and y -register. Such a gate cannot change the bond dimension of the MPS by more than a factor of four. While we have not plotted the results for the Gray-code indexing in Fig. 2 to avoid overcrowding the figure, plotting the results would yield results similar to the other indexing variants.

⁴ This statement can be made more precise if the function $F(\mathbf{x})$, $\mathbf{x} \equiv (x, y)$, or its m th derivatives, are μ -Hölder continuous. Then, the Fourier coefficients $\hat{F}(\mathbf{k})$, $\mathbf{k} \equiv (k, \ell)$, decay as $\mathcal{O}(1/|\mathbf{k}|^{\mu+m})$ [77, Theorem 3.3.9]. Since $\sin(x)$ and $\cos(x)$ are analytic functions, also $\sin(F(\mathbf{x}))$ and $\cos(F(\mathbf{x}))$, or their m th derivatives, are μ -Hölder continuous and their Fourier coefficients also decay as $\mathcal{O}(1/|\mathbf{k}|^{\mu+m})$. Note that this bound is not necessarily asymptotically tight, at least in one dimension this decay can be further improved, e.g., to a faster decay as $\mathcal{O}(1/|k|^{1+\mu+m})$ if the function is not infinitely oscillatory [78, Theorem 1.1], or to include functions whose m th derivative is only piecewise continuously differentiable leading to a decay $\mathcal{O}(1/|k|^{1+m})$ [79, Theorem 5].

The amplitudes of one copy would be zero for each black pixel and $1/2^n$ for each white pixel, and the other way around for the other copy. Since the amplitudes are either zero or a constant, they can be represented as the sum of several rectangle functions. Taking the Fourier transform of this gives the sum of several scaled functions of the form $\text{sinc}(k) = \sin(k)/k$, which asymptotically decay as $\mathcal{O}(1/k)$. This means the decay of the Fourier coefficients is too slow and we cannot apply the arguments of the previous section to argue for a good MPS approximation. We thus expect a much larger approximation error, which is what we observed numerically in Fig. 2b.

As a side note, instead of Fourier transforms we could also consider cosine transforms, which are typically more commonly used in image processing (e.g., in the JPEG compression algorithm) than the usual Fourier transform. Since the cosine transforms can be related to Fourier transforms, we can apply the same error bounds—we make this connection precise in App. C.

Finally, we briefly want to comment on the entanglement entropy of these states. For states using amplitude encoding or the FRQI, the error of the MPS approximation decays algebraically with exponent larger than one. From this, one can estimate the decay of the Schmidt values, which is the same asymptotically. This means that the Schmidt values decay fast enough so that even as the system size tends to infinity the bipartite entanglement remains bounded, which explains the behavior observed in Fig. 2a; since the NEQR does not admit such an efficient MPS representation, but still has more structure than a random state, it makes sense that the entanglement entropy is somewhere in between the two cases (see Fig. 2a). The small entanglement entropy of these states is a useful property for machine learning tasks, besides making them efficiently preparable as input states on a quantum computer. Consider a classification task, where we first prepare an initial state that encodes the input data, we then run a circuit that implements a classification algorithm, and finally we measure a few qubits to assign a classification label based on the most likely bitstring outcome. To find this bitstring with only a few shots on a quantum computer, we want there to be a big difference in the probability between the most likely and the second most likely outcome. If the qubits we measure are highly entangled with the rest of the system, their reduced density matrix will be close to an identity matrix, and so all bitstrings will have roughly the same measurement probability. Since this is exactly the case we want to avoid, we want the measured qubits to only be weakly entangled with the rest of the system. This means, the classification algorithm must disentangle the qubits that are to be measured from the rest of the system. As unitarily disentangling a state is generically a hard problem if the circuit that created the state is unknown [80–82], and we want the classification circuit to be efficient, i.e., to use as little gates as possible, this is only possible if the input state is already only weakly entangled. In this sense, the states discussed here are well-suited as input

states for machine learning tasks. Of course, for there to be any hope of quantum advantage, some intermediate step of the classification circuit must make the state highly entangled, so that it is no longer classically simulable.

IV. IMAGE COMPRESSION WITH CIRCUITS

In the previous section we discussed that typical quantum states representing classical image data can be well-approximated by MPS. This means they are quite different from generic quantum states in the Hilbert space, for which an exponentially deep circuit is needed for the preparation on a quantum computer [15, 16]. Here, we discuss how this special structure of the quantum states can lead to more efficient linear-depth circuits for state preparation, and how to obtain them.

A. Sequential circuits from MPS

We can directly turn an MPS with bond dimension χ into a sequential quantum circuit with $\mathcal{O}(\chi^2 n)$ two-qubit gates [24–29]. Such a circuit is shown in Fig. 6a for $\chi = 4$, where each $\chi \times 2 \times \chi$ MPS tensor gets mapped to a $\log_2(\chi) + 1$ -qubit gate, with one incoming qubit in the state $|0\rangle$, one outgoing qubit corresponding to the physical leg of the MPS, and the remaining $\log_2(\chi)$ quantum wires corresponding to the virtual legs of the MPS. Since we have seen in the previous section that the bond dimension scales as $\mathcal{O}(\log(1/\epsilon))$ or $\mathcal{O}\left((1/\epsilon)^{1/(\min(\alpha,\beta)-\frac{1}{2})}\right)$, depending on whether the Fourier coefficients decay exponentially or algebraically, the scaling of the number of gates becomes $\mathcal{O}(n \log(1/\epsilon)^2)$ or $\mathcal{O}\left(n (1/\epsilon)^{2/(\min(\alpha,\beta)-\frac{1}{2})}\right)$, respectively. In both cases the complexity of the circuit reduces from a scaling exponential in n to a scaling linear in n , compared to the exact state preparation.

The question remains, however, how to obtain the MPS in practice. In practice, a popular algorithm to obtain an MPS from a quantum state that yields good results is to iteratively perform a SVD on each bond, and only keep the χ dominant singular values [68]. Since the SVD of an $\ell \times m$ matrix has a computational complexity of $\mathcal{O}(\ell m \min(\ell, m))$, and we need to do SVDs of $\min(2^i, \chi, 2^{2n-i+1}) \times 2^{2n-i}$ -matrices, where the index i runs over each of the $\mathcal{O}(n)$ bonds, the cost of this method scales as $\mathcal{O}(\chi^2 2^{2n})$.⁵ As the bond dimension does not scale asymptotically with n , this is asymptotically slightly better than the the classical preprocessing of $\mathcal{O}(n 2^{2n})$ needed to obtain the exact state preparation circuit with the least gates (see Sec. II). More importantly, asymptotically the circuit preparing the approximate state needs exponentially fewer gates.

Instead of doing the SVD, one could also try to actually do the Fourier transform, truncate the spectrum of

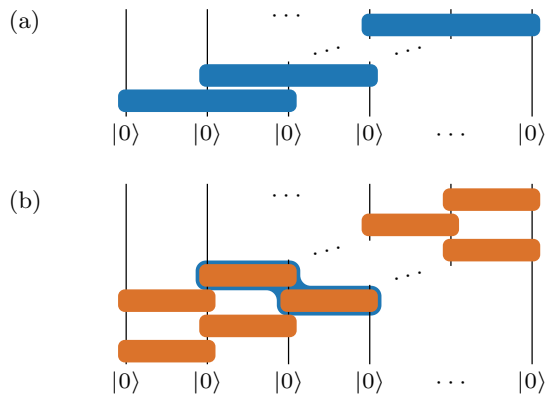


FIG. 6. (a) **MPS circuit** and (b) **compressed sequential circuit**. (a) A circuit consisting of gates that act on $\log_2(\chi) + 1$ qubits arranged in a sequential pattern is in one-to-one correspondence with an MPS of bond dimension χ —see e.g. Refs. [26, 28, 29, 83] for details of the mapping. The example shown here is for $\chi = 4$. (b) Instead of using multi-qubit gates, one can also repeat several layers of a circuit corresponding to a $\chi = 2$ MPS, shown here for two layers. The two gates framed by the blue box correspond to a sequentially repeated multi-qubit gate—in that sense, compressed sequential circuits can be viewed as a sparsely parametrized subclass of MPS circuits.

Fourier coefficients, and construct the MPS from that. The full DFT, however, will scale as $\mathcal{O}(n 2^{2n})$, which is slightly worse than doing the SVD, and will generically yield a worse MPS approximation. Instead of doing the full Fourier transform, one could instead perform a sparse two-dimensional Fourier transform (as suggested in Ref. [19]) to extract only the dominant Fourier modes [84–86]. There are several different implementations for different cases, but with one such implementation estimating the $\mathcal{O}(\chi^2)$ dominant Fourier coefficients of an $2^n \times 2^n$ -pixel image with success-probability $1 - \delta$ and error ϵ scales as $\mathcal{O}(\chi^2 \text{poly}(\log(1/\delta), n, 1/\epsilon))$ [84]. In principle this could get rid of the exponential scaling entirely, however, it should be examined carefully if real images satisfy the assumptions about the sparsity of the Fourier spectrum that is assumed in the proofs of these algorithms.

⁵ More explicitly, let us assume that $\chi = 2^\eta$ is some power of two and we have a $2n$ -qubit state, then the total cost for turning the state into an MPS by successive SVDs is given by

$$\begin{aligned}
 & \sum_{i=1}^{2n-1} \mathcal{O}(\min(2^i, \chi, 2^{2n-i+1})^2 2^{2n-i}) \\
 &= \sum_{i=1}^{\eta} \mathcal{O}(2^{2i} 2^{2n-i}) + \sum_{i=\eta+1}^{2n-1-\eta} \mathcal{O}(\chi^2 2^{2n-i}) \\
 & \quad + \sum_{i=2n-\eta}^{2n-1} \mathcal{O}((2^{2n-i+1})^2 2^{2n-i}) \\
 &= \mathcal{O}(\chi^2 2^{2n}) + \mathcal{O}(\chi^2 2^{2n}/\chi) + \mathcal{O}(\chi^3) = \mathcal{O}(\chi^2 2^{2n}).
 \end{aligned}$$

B. Compressed circuits

Directly turning the MPS approximation of an image state into a circuit yields a circuit which needs $\mathcal{O}(\chi^{2n})$ gates. This leads to a very efficient linear scaling asymptotically, as the bond dimension χ tends to a constant; however, in practice, the prefactor χ^2 can become very large and can render this approach unsuitable for the currently available noisy intermediate-scale quantum (NISQ) [87] devices. In this section, we present more NISQ-friendly circuits and variationally optimize them to approximate the image states, in a sense further compressing the circuits needed to approximately prepare the image states.

One-dimensional sequential circuits. One way to reduce the complexity of the circuit obtained directly from the MPS is to instead use several layers of a sequential circuit consisting of only two-qubit gates, which avoids a costly decomposition of the multi-qubit gates. An example for two layers is shown in Fig. 6b. In the figure, two gates are highlighted in blue, which act like a multi-qubit gate that is applied sequentially, just like in Fig. 6a. Therefore, we can equivalently view the circuit as replacing each dense multi-qubit gate, which would require $\mathcal{O}(\chi^2)$ two-qubit gates to implement, by a series of $\log_2(\chi)$ two-qubit gates—in that sense, the circuit is a sparse version of the full MPS circuit [28]. Numerically, it has been observed that for certain applications these compressed circuits work just as well as MPS [22, 28, 83]. The circuits can be obtained either variationally [22, 28] or by repeatedly disentangling the original MPS [88]. Using variational methods, one could, in principle, find the best sequential circuit with a fixed number of layers to approximate the target state, as long as one does not get stuck in local minima during the optimization. The optimization could also be done in a hybrid quantum-classical setup, where the circuit is evaluated on a quantum computer and the parameters are updated using some classical optimization scheme. In contrast, constructing the compressed circuit with a fixed number of layers using repeated disentangling gates will not generally converge to the best approximation; however, the computational cost on a classical computer is much lower and one can avoid variational optimization where the computational cost is hard to estimate.

Here, we focus on the variational approach to compress states encoding images (similarly to Ref. [22]). We take the first 1000 images of the Fashion-MNIST dataset [43], resize them from the original 28×28 pixels to 32×32 pixels, and then map them to quantum states using amplitude encoding, the FRQI and the NEQR with 1–3 color qubits with snake indexing. We then optimize compressed sequential circuits (as in Fig. 6b) with 1–3 layers to approximate the states. The average infidelities of the optimized circuits and the original states are plotted against the number of variational parameters of the circuit in Fig. 9. The blue crosses in the left plot show the results for amplitude encoding, the orange crosses in the

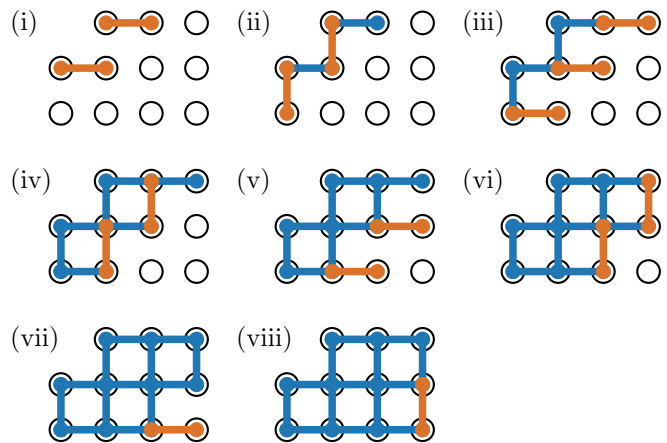


FIG. 7. **Constructing a two-dimensional sequential circuit.** Sequential circuits can also be constructed in two dimensions [89]. At each step, the orange gates show the newly applied gates, and the blue gates show the ones that have been applied previously. The sequentially repeating pattern here consists of gates along a diagonal, which are applied alternately horizontally or vertically.

central plot show the results for the FRQI and the green crosses in the right plot show the results for the NEQR. The shaded area shows the 25th–75th percentiles. Note that the number of parameters in the variational circuit differs between the different encodings even when the circuit has the same number of layers because the number of qubits changes.

Two-dimensional sequential circuits. Sequential circuits can not only be implemented in one dimension, but also in higher dimensions [89]. Since many superconducting quantum devices have their qubits arranged in a two-dimensional lattice, we will focus on this case. In two dimensions, sequential circuits form a subclass of general two-dimensional tensor networks [89, 90], which with a fixed bond dimension can create entanglement entropies following a two-dimensional area law. Conversely, to create a state with an area law in two dimensions using MPS, the bond dimension needs to grow exponentially. Thus, two-dimensional sequential circuits can in principle be a more powerful ansatz than one-dimensional sequential circuits, and we can hope that this also leads to a better approximation of quantum states encoding classical image data.

To test this, we construct a circuit as shown in Fig. 7. There, we have eleven qubits arranged in a 3×4 square lattice with the top left qubit removed. This corresponds e.g. to the case of encoding a 32×32 -pixel image using the FRQI. At each step of the construction, the gates applied in the current step are shown in orange, and the gates applied in previous steps are shown in blue. We start the construction by first applying two-qubit gates horizontally along the top-left-most diagonal, and then applying two-qubit gates vertically along the same diagonal. This procedure is then repeated sequentially on

the next diagonals, moving diagonal by diagonal to the bottom right. For different system sizes the construction works analogously. Similar to the case of the one-dimensional compressed sequential circuit, we can view this construction as a single layer, and repeat it several times to obtain sequential circuits with several layers.

As for the one-dimensional sequential circuit, we encode the first 1000 images of the Fashion-MNIST dataset [43] using the three encodings discussed in Sec. II with snake indexing, and optimize the circuit with 1–3 layers to approximate the corresponding quantum states. Since the number of qubits changes for the different encodings, we use different layouts for the qubits. The amplitude encoding uses ten qubits, which we lay out in a 4×4 grid, with all qubits above the diagonal from bottom-left to top-right removed; the FRQI and the NEQR with a single color qubit use eleven qubits, which corresponds to the case shown in Fig. 7; the NEQR with two color qubits uses twelve qubits, which we can arrange in a 3×4 grid without removing any qubits; and the NEQR with three color qubits uses thirteen qubits, which we arrange in a 4×4 grid with the three qubits in the top-left corner removed. The resulting infidelities of the approximation are plotted in Fig. 9 against the number of variational parameters in the circuit. The blue pluses in the left plot show the results for the amplitude encoding, the orange pluses in the central plot show the results for the FRQI, and the green pluses in the right plot show the results for the NEQR. The shaded area shows the 25th–75th percentiles.

MERA circuit. Another tensor network that can be turned into a quantum circuit is the multi-scale entanglement renormalization ansatz (MERA) [91]. (In the QML literature such a circuit is also known as a quantum convolutional neural network or QCNN [9].) The idea of the MERA is to perform a kind of coarse-graining in the entanglement structure of the state and to subsequently reduce the number of qubits in the system. At each step the qubits are grouped into two-site unit cells. Then, a unitary tensor is applied to all neighboring qubits in different unit cells in order to disentangle the different unit cells. Then, an isometric tensor is applied within each unit cell, mapping each two-qubit state to a single-qubit state. This procedure can be repeated until there are only two qubits left in the system. Running this renormalization in reverse constructs a quantum state, and since all tensors are isometric, it can be written as a quantum circuit. Such a circuit is shown in Fig. 8, where the isometries that double the number of qubits are shown in orange, and the entangling operations between the unit cells are shown in blue. Due to its hierarchical structure, the circuit can build up correlations and entanglement at all length scales, and is therefore able to describe states with an entanglement entropy that grows logarithmically in the number of qubits, which one-dimensional sequential circuits with a fixed number of layers are unable to replicate.

Here we view the MERA circuit as a variational ansatz,

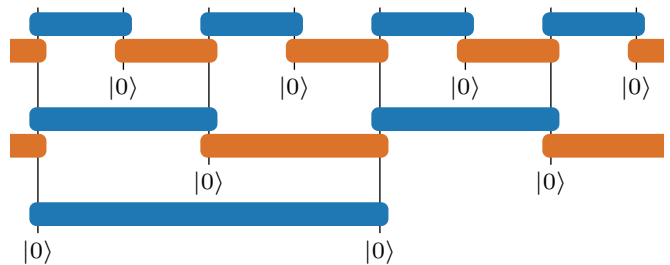


FIG. 8. **MERA circuit.** Since the MERA [91] consists of isometric tensors, the tensor network with bond dimension $\chi = 2$ can be naturally expressed as a quantum circuit. With each layer, the number of qubits is doubled by inserting a qubit in between the qubits of the previous layer and then entangling it with its nearest neighbors (indicated by the orange and blue gates). This way, entanglement is built up over all length scales of the system.

and optimize the gates in the circuit to best approximate quantum states representing image data. Since the number of qubits of these quantum states is usually not a perfect power of two, we need to slightly adapt the construction of the MERA circuit. If at any layer the number of qubits is even, the construction proceeds as described above and we assume periodic boundary conditions when it comes to disentangling the different unit cells. If at any layer there is an odd number of qubits, we split all qubits into pairs as before except that the last qubit remains without a partner. Then we apply the disentanglers between the unit cells such that the unpaired qubit is disentangled from the last unit cell, and no gate acts on the first qubit. The isometries are applied within the unit cell, which means at this step no gate is applied to the unpaired qubit. This way we have reduced the number of qubits, and can repeat the steps above until only two qubits are left. Running this structure in reverse creates a MERA-like circuit for a number of qubits that is not a power of two. To increase the expressiveness of the MERA with a fixed system size on a classical computer, one usually increases the matrix dimensions of the intermediate isometries in the ansatz. However, this is not so straightforward to do on a quantum computer, so we restrict to a fixed number of parameters of the MERA for a given number of qubits.

As before, we variationally optimize the circuits to approximate the states encoding the first 1000 images of the Fashion-MNIST dataset [43], which yields the infidelities shown in Fig. 9. The average infidelity for the states using amplitude encoding is shown on the left plot as a blue dot, the average infidelity for the FRQI is shown in the central plot as an orange dot, and the average infidelities for the NEQR with 1–3 color qubits are shown in the right plot as green dots. The error bars show the 25th–75th percentiles.

Comparing the results in Fig. 9 between the different circuit ansätze shows that there is not a big difference in the achievable infidelities. For a given encoding,

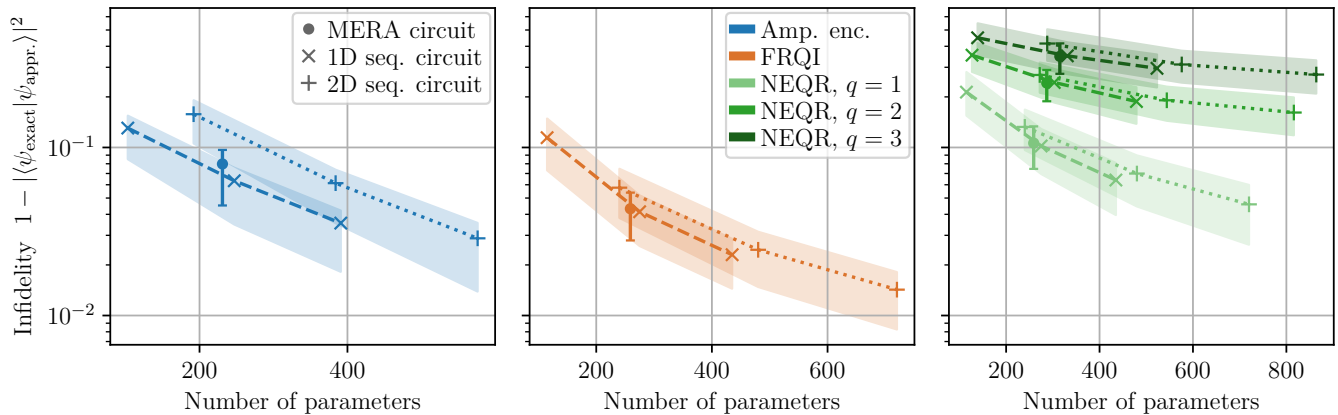


FIG. 9. **Comparison of approximation error for different circuit types.** The first 1000 images of the Fashion-MNIST dataset [43] are encoded using snake indexing in combination with amplitude encoding (left, in blue), the FRQI (center, in orange) and the NEQR with 1–3 color qubits (right, in green). The data shown are the average infidelities of the original state and the variationally optimized circuit, plotted against the number of parameters in the circuit. We show results for a MERA circuit (see Fig. 8) as dots, for the one-dimensional compressed sequential circuit (see Fig. 6b) as crosses and for the two-dimensional sequential circuit (see Fig. 7) as pluses. The error bars and the shaded area show the 25th–75th percentiles.

the infidelities seem to depend mostly on the number of variational parameters in the circuit and almost not at all on the type of circuit used in the optimization. This seems a bit surprising at first, since in principle the MERA circuit and the two-dimensional sequential circuit are more powerful ansätze—the first being able to describe critical systems with a logarithmically increasing entanglement entropy [91] and the second being able to capture an area law for the entanglement entropy in two dimensions [89, 90]. The observation that these circuits do not perform significantly better suggests that the entanglement structure of quantum states encoding classical image data is adequately captured by MPS or one-dimensional sequential circuits. This is in agreement with the results we derived in Sec. III. In a sense, this means the two-dimensional structure of the image as classical data gets lost once it gets mapped to a quantum state, where now the correlations between the qubits correspond to correlations between different length-scales, which are well described by a one-dimensional ansatz circuit.

V. CONCLUSION

We have considered three different encodings for mapping two-dimensional classical data to a quantum state, i.e., amplitude encoding, the FRQI and the NEQR. If one can view the data as being equidistant samples from a function with continuous inputs whose Fourier coefficients decay faster than $\mathcal{O}(|k|^{-1}|\ell|^{-1})$, we have shown that the states obtained from amplitude encoding or the FRQI can be efficiently approximated by MPS, in the sense that the bond dimension does not scale asymptotically with the size of the input data. This MPS-

representation directly leads to a circuit with a number of gates that, in the worst case, scales as $\mathcal{O}(n/\epsilon^4)$, i.e., only linearly in the number of qubits. The exponent of the scaling with the approximation error becomes smaller if the Fourier coefficients decay faster. We have explained why for the NEQR such an MPS approximation is not as efficient, however, numerically we found it to still work better than for generic states. Moreover, we have considered one- and two-dimensional compressed sequential circuits as well as a MERA circuit as variational ansätze to compress quantum states representing classical image data, and found that even though the other circuit ansätze are more powerful in principle, the one-dimensional circuits are capable of achieving the same fidelities with the same number of parameters. This further suggests that the relevant entanglement structure of these states is captured by MPS.

Our results prove a slightly modified version of the conjecture in Refs. [20, 21]. Ref. [20] showed that encoding a probability distribution with a bounded derivative in the amplitudes of an n -qubit state, and adding a single qubit in order to double the resolution, only introduces an entanglement entropy of the order $\mathcal{O}(2^{-m})$ between the newly added qubit and the previous qubits. Based on this result, and numerical evidence in Refs. [20, 21], it was conjectured that also higher-dimensional real-valued functions with a bounded derivative can be efficiently approximated by MPS. Here we proved this for two-dimensional complex-valued functions with sufficiently quickly decaying Fourier coefficients, which also includes functions where the derivative is not bounded. Our results also give theoretical justification for the observation in Ref. [22], that FRQI states can be well approximated by MPS with a small bond dimension and sequential circuits with only a few layers.

An open question remains how to best obtain the MPS approximation in practice. Using the SVD yields a high-fidelity MPS approximation with a cost of $\mathcal{O}(2^{2n})$, which is slightly better than the classical preprocessing with cost $\mathcal{O}(n2^{2n})$ needed for finding the optimal circuit that exactly prepares the state [17] (while also yielding a circuit with exponentially fewer gates); however, the scaling is still exponential in the number of qubits. A full reduction from the exponential scaling seems unlikely if all exponentially many pixels are supposed to be processed to find an approximation. In principle, it might be possible to circumvent the exponential scaling either via stochastic methods like the sparse Fourier transform [84–86] or stochastic SVDs [92–94], or via interpolation methods like the tensor cross interpolation [39, 40, 95–97]. In practice, the classical data we are dealing with still needs to be stored on a classical computer, so the size of the input data cannot be intractably large. For those cases, the usual SVD could suffice for finding good linear-depth circuit approximations, and there might still be a relevant speedup in processing the dataset classically in this way first, before further processing the dataset on a quantum computer. Especially for NISQ devices, this could turn exponential-depth circuits that cannot be run on the quantum hardware into linear-depth circuits that can be run on the quantum hardware and thus allows to retain some of the advantages of a quantum computer.

Here, our focus has been on finding circuits for efficiently preparing quantum states that describe classical input data, but with a clear application to QML in mind. A natural question is thus if we can also find circuits that efficiently classify input data that was prepared in this way? At least for small images, Ref. [22] found that using the same sequential circuit structure for learning the classification task as for the data preparation works well, but the question whether this observation scales to larger system sizes remains open. The successful application of MPS-based algorithms to classical machine learning tasks suggests that the MPS-inspired sequential circuits can also scale to larger systems, however, the types of image encodings used in these applications usually differ significantly from the encodings considered here [98–101]. Other popular circuits for data classification use the structure of a MERA circuit (and are also often called QCNNs in this context) [9, 10, 102]. As discussed previously, MERA circuits can in principle be more powerful than one-dimensional sequential circuits in terms of the entanglement entropy they can create; however, they require the implementation of long-range two-qubit gates, and thus the best suited circuit for a classification task may also depend on the underlying quantum hardware. An advantage that both sequential circuits (up to a logarithmic number of layers) and MERA circuits share over the more conventional linear-depth brick wall circuits is that, for local cost functions, they do not suffer from barren plateaus [103–106].

ACKNOWLEDGMENTS

The authors thank Yu-Jie Liu, Michael Lubasch and Adam Smith for insightful discussions, and Lukas Lechner for generously granting permission to use their photograph in Fig. 3. F.P. thanks Rohit Dilip, Yu-Jie Liu and Adam Smith for collaboration on a related previous project. The optimization of the variational quantum circuits was implemented using the QGOpt library [107–109] and TensorFlow [110]. This research was funded by the BMW Group. C.A.R. and E.S. are partly funded by the German Ministry for Education and Research (BMB+F) in the Project QAI2-Q-KIS under Grant 13N15583. F.P. acknowledges the support of the Deutsche Forschungsgemeinschaft (DFG, German Research Foundation) under Germany’s Excellence Strategy EXC-2111-390814868, the European Research Council (ERC) under the European Union’s Horizon 2020 research and innovation program (grant agreement No. 771537), as well as the Munich Quantum Valley, which is supported by the Bavarian state government with funds from the Hightech Agenda Bayern Plus.

Data and materials availability: Data analysis and simulation codes are available on Zenodo upon reasonable request [111].

Appendix A: Constructing an MPS from two-dimensional Fourier modes

In the main text we claimed that a state whose amplitudes are given by a two-dimensional Fourier transform containing only a $\chi \times \chi$ matrix of Fourier coefficients can be written as an MPS with bond dimension χ . Here we proof this claim.

We consider a $2n$ -qubit state whose amplitudes (up to normalization) are given by the $2^n \times 2^n$ matrix f_{ab} as

$$|\psi\rangle \propto \sum_{a,b=0}^{2^n-1} f_{ab} |b\rangle |a\rangle, \quad (\text{A1})$$

where the basis states $|b\rangle$ live on the first register of n qubits and label the y -coordinate of the image, and the basis states $|a\rangle$ live on the second register of n qubits and label the x -coordinate. The matrix f_{ab} , by assumption, can be written in terms of a $\chi \times \chi$ matrix of Fourier coefficients \hat{f}_{pq} as

$$f_{ab} = \sum_{p,q=0}^{\chi-1} \hat{f}_{pq} e^{i2\pi pa/2^n} e^{i2\pi qb/2^n}. \quad (\text{A2})$$

Expressing the two summation indices in terms of n -bit binaries, $a = \sum_{j=0}^{n-1} 2^{n-1-j} \sigma_j$ and $b = \sum_{j=0}^{n-1} 2^{n-1-j} \sigma'_j$,

we have

$$\begin{aligned}
|\psi\rangle &\propto \sum_{a,b=0}^{2^n-1} \sum_{p,q=0}^{\chi-1} \hat{f}_{pq} e^{i2\pi pa/2^n} e^{i2\pi qb/2^n} |b\rangle|a\rangle \\
&= \sum_{\{\sigma_j\}} \sum_{\{\sigma'_j\}} \sum_{p,q=0}^{\chi-1} \left(\prod_{j=0}^{n-1} e^{i2\pi q\sigma_j/2^{j+1}} \right) \\
&\quad \times \hat{f}_{pq} \left(\prod_{j'=0}^{n-1} e^{i2\pi p\sigma'_{j'}/2^{j'+1}} \right) \\
&\quad \times |\sigma_0, \sigma_1, \dots, \sigma_{n-1}\rangle |\sigma'_0, \sigma'_1, \dots, \sigma'_{n-1}\rangle.
\end{aligned} \tag{A3}$$

This defines the following set of MPS tensors: for the first n qubits ($0 \leq j \leq n-1$) we have

$$A_{\alpha_j \alpha_{j+1}}^{[j] \sigma_j} = \delta_{\alpha_j, \alpha_{j+1}} e^{i2\pi \alpha_{j+1} \sigma_j / 2^{j+1}}, \tag{A4}$$

the states in the two n -qubit registers are connected by the matrix

$$C_{\alpha_{n-1} \beta_0} = \sum_{p,q=0}^{\chi-1} \delta_{\alpha_{n-1}, q} \hat{f}_{pq} \delta_{p, \beta_0}, \tag{A5}$$

and for the second n qubits we have

$$B_{\beta_j \beta_{j+1}}^{[n+j] \sigma'_j} = \delta_{\beta_j, \beta_{j+1}} e^{i2\pi \beta_{j+1} \sigma'_j / 2^{j+1}}; \tag{A6}$$

the indices α_0 and β_n are dummy indices that take only the value 0, the remaining indices all run from 0 to $\chi-1$.⁶ The amplitudes $\psi_{\sigma_0, \dots, \sigma_{n-1}, \sigma'_0, \dots, \sigma'_{n-1}}$ of the state (up to normalization) can then be written as an MPS with bond dimension χ as

$$\psi_{\sigma_0, \dots, \sigma_{n-1}, \sigma'_0, \dots, \sigma'_{n-1}} \propto A^{[0] \sigma_0} \dots A^{[n-1] \sigma_{n-1}} C B^{[n] \sigma'_0} \dots B^{[2n-1] \sigma'_{n-1}}, \tag{A7}$$

where we omit the virtual indices of the tensors and the matrix product is implied. See also Fig. 5a for a diagrammatic representation.

This construction also works if there is not a symmetric cutoff Λ in both directions, or if the contributing Fourier coefficients do not form a contiguous region of frequencies—as long as only a finite number of Fourier coefficients \hat{f}_{pq} contribute. The bond dimension χ_l of the MPS in the left half of the system, i.e., the σ_j qubit register, is the number of values q for which there exists a nonzero \hat{f}_{pq} . The bond dimension χ_r of the MPS in the right half of the system, i.e., the σ'_j qubit register, is the number of values p for which there exists a nonzero \hat{f}_{pq} .

⁶ In the tensor network literature the symbols A and B are often used to denote left- or right-isometric tensors. Here, we use the different symbols purely to differentiate the two halves of the system, and the tensors are not in left- or right-isometric form.

Appendix B: Proof of the approximation error bounds

In this section we give the detailed calculations for the error bounds that were presented in the main text.

First, we need to prove Eq. (18) in the main text; given two quantum states

$$|f\rangle = \frac{1}{\|f\|_F} \sum_{a,b=0}^{2^n-1} f_{ab} |b\rangle|a\rangle \tag{B1}$$

and

$$|g\rangle = \frac{1}{\|g\|_F} \sum_{a,b=0}^{2^n-1} g_{ab} |b\rangle|a\rangle, \tag{B2}$$

where $\|f\|_F = \sqrt{\sum_{a,b=0}^{2^n-1} |f_{ab}|^2}$ denotes the Frobenius norm of the matrix f , the norm of the difference between the two states can be written as

$$\begin{aligned}
\| |f\rangle - |g\rangle \|_2 &= \left\| \sum_{a,b=0}^{2^n-1} \left(\frac{f_{ab}}{\|f\|_F} - \frac{g_{ab}}{\|g\|_F} \right) |b\rangle|a\rangle \right\|_2 \\
&= \left\| \frac{f}{\|f\|_F} - \frac{g}{\|g\|_F} \right\|_F \\
&= \left\| \frac{f\|g\|_F - g\|f\|_F}{\|f\|_F \|g\|_F} \right\|_F \\
&= \left\| \frac{f(\|g\|_F - \|f\|_F) + (f-g)\|f\|_F}{\|f\|_F \|g\|_F} \right\|_F \\
&\leq \frac{\|f\|_F \|\|g\|_F - \|f\|_F\| + \|f-g\|_F \|f\|_F}{\|f\|_F \|g\|_F} \\
&\leq \frac{2\|f-g\|_F}{\|g\|_F}.
\end{aligned} \tag{B3}$$

To get to the last line we used the reverse triangle inequality $\| \|x\| - \|y\| \| \leq \|x - y\|$, which is a consequence of the usual triangle inequality.

1. Exponentially decaying Fourier coefficients

Here, we will assume an exponential decay of the Fourier coefficients $\hat{F}(k, \ell)$ in Eq. (7)—i.e., of the Fourier coefficients of the function $F(x, y)$ which takes continuous inputs x and y from which the pixelated data is obtained via sampling at discrete points and not the DFT coefficients \hat{f}_{pq} of pixelated data f_{ab} directly—and will relate them to the Fourier coefficients of a $2^n \times 2^n$ -pixel image. Then, we can calculate the error we make by only including Fourier coefficients up to some cutoff Λ , and how this error scales with the number of pixels 2^{2n} .

Consider Fourier coefficients that fulfill

$$|\hat{F}(k, \ell)| \leq C e^{-\alpha|k|} e^{-\beta|\ell|}, \tag{B4}$$

with some constants $C, \alpha, \beta > 0$.⁷ Using Eq. (9), we can bound the absolute value of the Fourier coefficients of a $2^n \times 2^n$ -pixel image, which yields

$$\begin{aligned} |\hat{f}_{pq}| &\leq \sum_{i,j \in \mathbb{Z}} |\hat{F}(p + i2^n, q + j2^n)| \leq C \left(\sum_{i \in \mathbb{Z}} e^{-\alpha|p+i2^n|} \right) \left(\sum_{j \in \mathbb{Z}} e^{-\beta|q+j2^n|} \right) \\ &= C \left(e^{-\alpha|p|} + (e^{\alpha p} + e^{-\alpha p}) \sum_{i=1}^{\infty} e^{-\alpha 2^n i} \right) \left(e^{-\beta|q|} + (e^{\beta q} + e^{-\beta q}) \sum_{j=1}^{\infty} e^{-\beta 2^n j} \right) \\ &= C \left(e^{-\alpha|p|} + (e^{\alpha p} + e^{-\alpha p}) \frac{e^{-\alpha 2^n}}{1 - e^{-\alpha 2^n}} \right) \left(e^{-\beta|q|} + (e^{\beta q} + e^{-\beta q}) \frac{e^{-\beta 2^n}}{1 - e^{-\beta 2^n}} \right). \end{aligned} \quad (\text{B5})$$

To calculate the error in Eq. (19) we need to evaluate $\|\hat{f} - \hat{g}\|_2$ as given in Eq. (20), which sums over the set of discarded Fourier coefficients. We can write this sum over I_{disc} as the difference of sums over the set of all Fourier coefficients I_{all} and the set over the kept Fourier coefficients I_{appr} ,

$$\sum_{(p,q) \in I_{\text{disc}}} |\hat{f}_{pq}|^2 = \sum_{(p,q) \in I_{\text{all}}} |\hat{f}_{pq}|^2 - \sum_{(p,q) \in I_{\text{appr}}} |\hat{f}_{pq}|^2, \quad (\text{B6})$$

and then insert the result from Eq. (B5) for $|\hat{f}_{pq}|$. From Eq. (B5) we have for the square of $|\hat{f}_{pq}|$ that

$$\begin{aligned} |\hat{f}_{pq}|^2 &\leq C^2 \left(e^{-2\alpha|p|} + 2 \frac{1 + e^{-2\alpha|p|}}{e^{\alpha 2^n} - 1} + \frac{2 + e^{2\alpha p} + e^{-2\alpha p}}{(e^{\alpha 2^n} - 1)^2} \right) \\ &\quad \times \left(e^{-2\beta|p|} + 2 \frac{1 + e^{-2\beta|p|}}{e^{\beta 2^n} - 1} + \frac{2 + e^{2\beta p} + e^{-2\beta p}}{(e^{\beta 2^n} - 1)^2} \right). \end{aligned} \quad (\text{B7})$$

We first consider the sum over I_{all} in Eq. (B6), and can perform the sums over p and q individually. There are three terms that contribute to the sum over p —for the first term we have

$$\sum_{p=-2^{n/2}}^{2^{n/2}-1} e^{-2\alpha|p|} = (1 + e^{-2\alpha}) \sum_{p=0}^{2^{n/2}-1} e^{-2\alpha p} = (1 + e^{-2\alpha}) \frac{1 - e^{-2\alpha 2^{n/2}}}{1 - e^{-2\alpha}} = \coth(\alpha) (1 - e^{-\alpha 2^n}), \quad (\text{B8})$$

where we have used the geometric sum; for the second term we have

$$\sum_{p=-2^{n/2}}^{2^{n/2}-1} 2 \frac{1 + e^{-2\alpha|p|}}{e^{\alpha 2^n} - 1} = 2 \frac{2^n + \coth(\alpha) (1 - e^{-\alpha 2^n})}{e^{\alpha 2^n} - 1} = 2 \frac{2^n}{e^{\alpha 2^n} - 1} + 2 \coth(\alpha) e^{-\alpha 2^n}, \quad (\text{B9})$$

where we have used the result for the first term; and, finally, for the third term we have

$$\begin{aligned} \sum_{p=-2^{n/2}}^{2^{n/2}-1} \frac{2 + e^{2\alpha p} + e^{-2\alpha p}}{(e^{\alpha 2^n} - 1)^2} &= 2 \frac{2^n}{(e^{\alpha 2^n} - 1)^2} + \frac{\coth(-\alpha) (1 - e^{\alpha 2^n})}{(e^{\alpha 2^n} - 1)^2} + \frac{\coth(\alpha) (1 - e^{-\alpha 2^n})}{(e^{\alpha 2^n} - 1)^2} \\ &= 2 \frac{2^n + \coth(\alpha) \sinh(\alpha 2^n)}{(e^{\alpha 2^n} - 1)^2}, \end{aligned} \quad (\text{B10})$$

where we have again used the results for the first term. Putting everything together, the result of the sum over p is

$$\begin{aligned} \sum_{p=-2^{n/2}}^{2^{n/2}-1} e^{-2\alpha|p|} + 2 \frac{1 + e^{-2\alpha|p|}}{e^{\alpha 2^n} - 1} + \frac{2 + e^{2\alpha p} + e^{-2\alpha p}}{(e^{\alpha 2^n} - 1)^2} &= \\ &= \coth(\alpha) (1 - e^{-\alpha 2^n}) + 2 \frac{2^n}{e^{\alpha 2^n} - 1} + 2 \coth(\alpha) e^{-\alpha 2^n} + 2 \frac{2^n + \coth(\alpha) \sinh(\alpha 2^n)}{(e^{\alpha 2^n} - 1)^2} \\ &= \coth(\alpha) \left(1 + e^{-\alpha 2^n} + \frac{\sinh(\alpha 2^n)}{(e^{\alpha 2^n} - 1)^2} \right) + \frac{2^n/2}{\sinh(\frac{\alpha}{2} 2^n)}. \end{aligned} \quad (\text{B11})$$

The results for the sum over q can be obtained in the same way by replacing α with β .

⁷ This bound on the Fourier coefficients is actually only important for frequencies larger than the cutoff Λ . The same error bounds hold for any structure of the Fourier coefficients within the cutoff, as the approximation error is given by the sum over the discarded Fourier coefficients and so the coefficients within the cutoff do not contribute.

Now we turn to the sum over I_{appr} ; we can again perform the sums over p and q separately, and three terms contribute. Defining $\chi = 2\Lambda + 1$, for the first term we have

$$\sum_{p=-\Lambda}^{\Lambda} e^{-2\alpha|p|} = 1 + 2e^{-2\alpha} \sum_{p=0}^{\Lambda-1} e^{-2\alpha p} = 1 + 2e^{-2\alpha} \frac{1 - e^{-2\alpha\Lambda}}{1 - e^{-2\alpha}} = \coth(\alpha) - \frac{e^{-\alpha\chi}}{\sinh(\alpha)}; \quad (\text{B12})$$

for the second term we have

$$\sum_{p=-\Lambda}^{\Lambda} 2 \frac{1 + e^{-2\alpha|p|}}{e^{\alpha 2^n} - 1} = 2 \frac{\chi + \coth(\alpha) - e^{-\alpha\chi}/\sinh(\alpha)}{e^{\alpha 2^n} - 1}; \quad (\text{B13})$$

and for the third term we have

$$\begin{aligned} \sum_{p=-\Lambda}^{\Lambda} \frac{2 + e^{2\alpha p} + e^{-2\alpha p}}{(e^{\alpha 2^n} - 1)^2} &= 2 \frac{\chi}{(e^{\alpha 2^n} - 1)^2} + \frac{\coth(-\alpha) - \frac{e^{\alpha\chi}}{\sinh(-\alpha)}}{(e^{\alpha 2^n} - 1)^2} + \frac{\coth(\alpha) - \frac{e^{-\alpha\chi}}{\sinh(\alpha)}}{(e^{\alpha 2^n} - 1)^2} \\ &= 2 \frac{\chi + \sinh(\alpha\chi)/\sinh(\alpha)}{(e^{\alpha 2^n} - 1)^2}. \end{aligned} \quad (\text{B14})$$

Putting everything together, the result of the sum over p is

$$\begin{aligned} \sum_{p=-\Lambda}^{\Lambda} e^{-2\alpha|p|} + 2 \frac{1 + e^{-2\alpha|p|}}{e^{\alpha 2^n} - 1} + \frac{2 + e^{2\alpha p} + e^{-2\alpha p}}{(e^{\alpha 2^n} - 1)^2} &= \\ &= \coth(\alpha) - \frac{e^{-\alpha\chi}}{\sinh(\alpha)} + 2 \frac{\chi + \coth(\alpha)}{e^{\alpha 2^n} - 1} - 2 \frac{e^{-\alpha\chi}/\sinh(\alpha)}{e^{\alpha 2^n} - 1} + 2 \frac{\chi + \sinh(\alpha\chi)/\sinh(\alpha)}{(e^{\alpha 2^n} - 1)^2} \\ &= \left(\coth(\alpha) - \frac{e^{-\alpha\chi}}{\sinh(\alpha)} \right) \left(1 + \frac{2}{e^{\alpha 2^n} - 1} \right) + \frac{\chi + e^{-\alpha 2^n} \sinh(\alpha\chi)/\sinh(\alpha)}{2 \sinh(\frac{\alpha}{2} 2^n)^2}. \end{aligned} \quad (\text{B15})$$

The results for the sum over q can be obtained in the same way by replacing α with β .

Taking the two results in Eqs. (B11) and (B15) and plugging them into Eq. (B6), we have

$$\begin{aligned} \sum_{(p,q) \in I_{\text{disc}}} |\hat{f}_{pq}|^2 &\leq C^2 \left(\coth(\alpha) \left(1 + e^{-\alpha 2^n} + \frac{\sinh(\alpha 2^n)}{(e^{\alpha 2^n} - 1)^2} \right) + \frac{2^n/2}{\sinh(\frac{\alpha}{2} 2^n)^2} \right) \\ &\quad \times \left(\coth(\beta) \left(1 + e^{-\beta 2^n} + \frac{\sinh(\beta 2^n)}{(e^{\beta 2^n} - 1)^2} \right) + \frac{2^n/2}{\sinh(\frac{\beta}{2} 2^n)^2} \right) \\ &\quad - C^2 \left(\left(\coth(\alpha) - \frac{e^{-\alpha\chi}}{\sinh(\alpha)} \right) \left(1 + \frac{2}{e^{\alpha 2^n} - 1} \right) + \frac{\chi + e^{-\alpha 2^n} \sinh(\alpha\chi)/\sinh(\alpha)}{2 \sinh(\frac{\alpha}{2} 2^n)^2} \right) \\ &\quad \times \left(\left(\coth(\beta) - \frac{e^{-\beta\chi}}{\sinh(\beta)} \right) \left(1 + \frac{2}{e^{\beta 2^n} - 1} \right) + \frac{\chi + e^{-\beta 2^n} \sinh(\beta\chi)/\sinh(\beta)}{2 \sinh(\frac{\beta}{2} 2^n)^2} \right). \end{aligned} \quad (\text{B16})$$

We can already see that the terms containing only $C^2 \coth(\alpha) \coth(\beta)$ without any χ - or 2^n -dependence will cancel, and all remaining terms either decay with χ or with 2^n . Since we are mostly interested in the asymptotic scaling, we can simplify this as

$$\begin{aligned} \sum_{(p,q) \in I_{\text{disc}}} |\hat{f}_{pq}|^2 &\leq C^2 \left(\coth(\alpha) + \mathcal{O}(2^n e^{-\alpha 2^n}) \right) \left(\coth(\beta) + \mathcal{O}(2^n e^{-\beta 2^n}) \right) \\ &\quad - C^2 \left(\left(\coth(\alpha) - \frac{e^{-\alpha\chi}}{\sinh(\alpha)} \right) + \mathcal{O}(\chi e^{-\alpha 2^n}) \right) \left(\left(\coth(\beta) - \frac{e^{-\beta\chi}}{\sinh(\beta)} \right) + \mathcal{O}(\chi e^{-\beta 2^n}) \right) \\ &= C^2 \left(\frac{\coth(\alpha)}{\sinh(\beta)} e^{-\beta\chi} + \frac{\coth(\beta)}{\sinh(\alpha)} e^{-\alpha\chi} + \frac{e^{-(\alpha+\beta)\chi}}{\sinh(\alpha) \sinh(\beta)} \right) + \mathcal{O}(2^n e^{-\alpha 2^n}, 2^n e^{-\beta 2^n}). \end{aligned} \quad (\text{B17})$$

This is the result presented in the main text.

2. Algebraically decaying Fourier coefficients

The more realistic case is when we assume the Fourier coefficients decay algebraically. The strategy for obtaining the error bounds is the same as for the exponential decay, except that some intermediate results cannot be simplified as nicely now. Consider Fourier coefficients that fulfill

$$|\hat{F}(k, \ell)| \leq C \frac{1}{(|k| + 1)^\alpha} \frac{1}{(|\ell| + 1)^\beta}, \quad (\text{B18})$$

with some constants $C > 0$ and $\alpha, \beta > 1$. Using Eq. (9), we can bound the absolute value of the Fourier coefficients of a $2^n \times 2^n$ -pixel image, which yields

$$\begin{aligned} |\hat{f}_{pq}| &\leq \sum_{i, j \in \mathbb{Z}} |\hat{F}(p + i2^n, q + j2^n)| \leq C \left(\sum_{i \in \mathbb{Z}} \frac{1}{(|p + i2^n| + 1)^\alpha} \right) \left(\sum_{j \in \mathbb{Z}} \frac{1}{(|q + j2^n| + 1)^\beta} \right) \\ &= C \left(\frac{1}{(|p| + 1)^\alpha} + \sum_{i=1}^{\infty} \frac{1}{(i2^n - p + 1)^\alpha} + \frac{1}{(i2^n + p + 1)^\alpha} \right) \left(\frac{1}{(|q| + 1)^\beta} + \sum_{j=1}^{\infty} \frac{1}{(j2^n - q + 1)^\beta} + \frac{1}{(j2^n + q + 1)^\beta} \right) \\ &= C \left(\frac{1}{(|p| + 1)^\alpha} + \frac{\zeta(\alpha, 1 + \frac{1-p}{2^n}) + \zeta(\alpha, 1 + \frac{1+p}{2^n})}{2^{n\alpha}} \right) \left(\frac{1}{(|q| + 1)^\beta} + \frac{\zeta(\beta, 1 + \frac{1-q}{2^n}) + \zeta(\beta, 1 + \frac{1+q}{2^n})}{2^{n\beta}} \right) \\ &= C \left(\frac{1}{(|p| + 1)^\alpha} + \frac{1}{2^{n\alpha}} (\zeta(\alpha, 1/2) + \zeta(\alpha, 1)) \right) \left(\frac{1}{(|q| + 1)^\beta} + \frac{1}{2^{n\beta}} (\zeta(\beta, 1/2) + \zeta(\beta, 1)) \right), \end{aligned} \quad (\text{B19})$$

where $\zeta(s, a) = \sum_{j=0}^{\infty} \frac{1}{(j+a)^s}$ is the Hurwitz zeta function and we have used that $\zeta(s, a) < \zeta(s, b)$ if $a > b$ [112].

To calculate the approximation error, we again need to sum $|\hat{f}_{pq}|^2$ over all discarded frequencies, and as in Eq. (B6) we split the sum into a difference of the sum over all frequencies and the sum over all retained frequencies. From Eq. (B19), we have for $|\hat{f}_{pq}|^2$ that

$$\begin{aligned} |\hat{f}_{pq}|^2 &\leq C^2 \left(\frac{1}{(|p| + 1)^{2\alpha}} + 2 \frac{\zeta(\alpha, 1/2) + \zeta(\alpha, 1)}{2^{n\alpha} (|p| + 1)^\alpha} + \frac{(\zeta(\alpha, 1/2) + \zeta(\alpha, 1))^2}{2^{n2\alpha}} \right) \\ &\quad \times \left(\frac{1}{(|q| + 1)^{2\beta}} + 2 \frac{\zeta(\beta, 1/2) + \zeta(\beta, 1)}{2^{n\beta} (|q| + 1)^\beta} + \frac{(\zeta(\beta, 1/2) + \zeta(\beta, 1))^2}{2^{n2\beta}} \right). \end{aligned} \quad (\text{B20})$$

First, we treat the sum over all frequencies. We can perform the sums over p and q separately, and three terms contribute to each sum. For the first term we have

$$\begin{aligned} \sum_{p=-2^{n/2}}^{2^{n/2}-1} \frac{1}{(|p| + 1)^{2\alpha}} &= (2^{n/2} + 1)^{-2\alpha} - 1 + 2 \sum_{p=0}^{2^{n/2}-1} \frac{1}{(|p| + 1)^{2\alpha}} \\ &= (2^{n/2} + 1)^{-2\alpha} - 1 + 2H_{2\alpha}(2^{n/2}) \\ &= 2\zeta(2\alpha, 1) - 1 + (2^{n/2} + 1)^{-2\alpha} - 2\zeta(2\alpha, 2^{n/2} + 1), \end{aligned} \quad (\text{B21})$$

where we have used the generalized harmonic numbers $H_s(n) = \sum_{j=1}^n \frac{1}{j^s}$ which relate to the Hurwitz zeta function as $H_s(n) = \zeta(s, 1) - \zeta(s, n+1)$ [112]; for the second term we have

$$\sum_{p=-2^{n/2}}^{2^{n/2}-1} 2 \frac{\zeta(\alpha, 1/2) + \zeta(\alpha, 1)}{2^{n\alpha} (|p| + 1)^\alpha} = 2 \frac{\zeta(\alpha, 1/2) + \zeta(\alpha, 1)}{2^{n\alpha}} \left(2\zeta(\alpha, 1) - 1 + (2^{n/2} + 1)^{-\alpha} - 2\zeta(\alpha, 2^{n/2} + 1) \right), \quad (\text{B22})$$

where we have used the result for the first term; and, finally, for the third term we have

$$\sum_{p=-2^{n/2}}^{2^{n/2}-1} \frac{(\zeta(\alpha, 1/2) + \zeta(\alpha, 1))^2}{2^{n2\alpha}} = \frac{(\zeta(\alpha, 1/2) + \zeta(\alpha, 1))^2}{2^{n(2\alpha-1)}}. \quad (\text{B23})$$

Putting everything together, the result of the sum over p is

$$\begin{aligned}
& \sum_{p=-2^{n/2}}^{2^{n/2}-1} \left(\frac{1}{(|p|+1)^{2\alpha}} + 2 \frac{\zeta(\alpha, 1/2) + \zeta(\alpha, 1)}{2^{n\alpha} (|p|+1)^\alpha} + \frac{(\zeta(\alpha, 1/2) + \zeta(\alpha, 1))^2}{2^{n2\alpha}} \right) = \\
& = 2\zeta(2\alpha, 1) - 1 + (2^{n/2} + 1)^{-2\alpha} - 2\zeta(2\alpha, 2^{n/2} + 1) \\
& + 2 \frac{\zeta(\alpha, 1/2) + \zeta(\alpha, 1)}{2^{n\alpha}} (2\zeta(\alpha, 1) - 1 + (2^{n/2} + 1)^{-\alpha} - 2\zeta(\alpha, 2^{n/2} + 1)) \\
& + \frac{(\zeta(\alpha, 1/2) + \zeta(\alpha, 1))^2}{2^{n(2\alpha-1)}}.
\end{aligned} \tag{B24}$$

The results for the sum over q can be obtained in the same way by replacing α with β .

Now we treat the sum over all retained frequencies. Again, we can perform the sums over p and q separately, and there are three terms that contribute. For the first term we have

$$\sum_{p=-\Lambda}^{\Lambda} \frac{1}{(|p|+1)^{2\alpha}} = 2 \sum_{p=0}^{\Lambda} \frac{1}{(|p|+1)^{2\alpha}} - 1 = 2H_{2\alpha}(\Lambda + 1) - 1 = 2\zeta(2\alpha, 1) - 2\zeta(2\alpha, \Lambda + 2) - 1; \tag{B25}$$

for the second term we have

$$\sum_{p=-\Lambda}^{\Lambda} 2 \frac{\zeta(\alpha, 1/2) + \zeta(\alpha, 1)}{2^{n\alpha} (|p|+1)^\alpha} = 2 \frac{\zeta(\alpha, 1/2) + \zeta(\alpha, 1)}{2^{n\alpha}} (2\zeta(\alpha, 1) - 2\zeta(\alpha, \Lambda + 2) - 1); \tag{B26}$$

and for the third term we have

$$\sum_{p=-\Lambda}^{\Lambda} \frac{(\zeta(\alpha, 1/2) + \zeta(\alpha, 1))^2}{2^{n2\alpha}} = (2\Lambda + 1) \frac{(\zeta(\alpha, 1/2) + \zeta(\alpha, 1))^2}{2^{n2\alpha}}. \tag{B27}$$

Putting everything together, the result of the sum over p is

$$\begin{aligned}
& \sum_{p=-\Lambda}^{\Lambda} \left(\frac{1}{(|p|+1)^{2\alpha}} + 2 \frac{\zeta(\alpha, 1/2) + \zeta(\alpha, 1)}{2^{n\alpha} (|p|+1)^\alpha} + \frac{(\zeta(\alpha, 1/2) + \zeta(\alpha, 1))^2}{2^{n2\alpha}} \right) = \\
& = 2\zeta(2\alpha, 1) - 2\zeta(2\alpha, \Lambda + 2) - 1 \\
& + 2 \frac{\zeta(\alpha, 1/2) + \zeta(\alpha, 1)}{2^{n\alpha}} (2\zeta(\alpha, 1) - 2\zeta(\alpha, \Lambda + 2) - 1) \\
& + (2\Lambda + 1) \frac{(\zeta(\alpha, 1/2) + \zeta(\alpha, 1))^2}{2^{n2\alpha}}.
\end{aligned} \tag{B28}$$

The results for the sum over q can be obtained in the same way by replacing α with β .

Taking the two results in Eqs. (B24) and (B28) and plugging them into Eq. (B6), we have

$$\begin{aligned}
\sum_{(p,q) \in I_{\text{disc}}} |\hat{f}_{pq}|^2 &\leq 4C^2 \left(\zeta(2\alpha, 1) - \frac{1}{2} + \frac{1}{2} (2^n/2 + 1)^{-2\alpha} - \zeta(2\alpha, 2^n/2 + 1) + \frac{(\zeta(\alpha, 1/2) + \zeta(\alpha, 1))^2}{2^{n(2\alpha-1)+1}} \right. \\
&\quad \left. + (\zeta(\alpha, 1) - \frac{1}{2} + \frac{1}{2} (2^n/2 + 1)^{-\alpha} - \zeta(\alpha, 2^n/2 + 1)) \frac{\zeta(\alpha, 1/2) + \zeta(\alpha, 1)}{2^{n\alpha-1}} \right) \\
&\quad \times \left(\zeta(2\beta, 1) - \frac{1}{2} + \frac{1}{2} (2^n/2 + 1)^{-2\beta} - \zeta(2\beta, 2^n/2 + 1) + \frac{(\zeta(\beta, 1/2) + \zeta(\beta, 1))^2}{2^{n(2\beta-1)+1}} \right. \\
&\quad \left. + (\zeta(\beta, 1) - \frac{1}{2} + \frac{1}{2} (2^n/2 + 1)^{-\beta} - \zeta(\beta, 2^n/2 + 1)) \frac{\zeta(\beta, 1/2) + \zeta(\beta, 1)}{2^{n\beta-1}} \right) \\
&\quad - 4C^2 \left(\zeta(2\alpha, 1) - \frac{1}{2} - \zeta(2\alpha, \Lambda + 2) + (\Lambda + \frac{1}{2}) \frac{(\zeta(\alpha, 1/2) + \zeta(\alpha, 1))^2}{2^{n2\alpha}} \right. \\
&\quad \left. + (\zeta(\alpha, 1) - \frac{1}{2} - \zeta(\alpha, \Lambda + 2)) \frac{\zeta(\alpha, 1/2) + \zeta(\alpha, 1)}{2^{n\alpha-1}} \right) \\
&\quad \times \left(\zeta(2\beta, 1) - \frac{1}{2} - \zeta(2\beta, \Lambda + 2) + (\Lambda + \frac{1}{2}) \frac{(\zeta(\beta, 1/2) + \zeta(\beta, 1))^2}{2^{n2\beta}} \right. \\
&\quad \left. + (\zeta(\beta, 1) - \frac{1}{2} - \zeta(\beta, \Lambda + 2)) \frac{\zeta(\beta, 1/2) + \zeta(\beta, 1)}{2^{n\beta-1}} \right). \tag{B29}
\end{aligned}$$

We can see that after expanding all brackets, the terms

$$\begin{aligned}
&4C^2 (\zeta(2\alpha, 1) - \frac{1}{2}) (\zeta(2\beta, 1) - \frac{1}{2}) \\
\text{and} \quad &4C^2 \frac{\zeta(\alpha, 1/2) + \zeta(\alpha, 1)}{2^{n\alpha-1}} (\zeta(\alpha, 1) - \frac{1}{2}) \frac{\zeta(\beta, 1/2) + \zeta(\beta, 1)}{2^{n\beta-1}} (\zeta(\beta, 1) - \frac{1}{2}) \tag{B30}
\end{aligned}$$

appear twice with opposite signs and will cancel. The remaining terms all either decay with 2^n or the cutoff Λ . Since we are interested in the asymptotic behavior for large n , we can simplify

$$\begin{aligned}
\sum_{(p,q) \in I_{\text{disc}}} |\hat{f}_{pq}|^2 &\leq 4C^2 \left(\zeta(2\alpha, 1) - \frac{1}{2} + (\zeta(\alpha, 1) - \frac{1}{2}) \frac{\zeta(\alpha, 1/2) + \zeta(\alpha, 1)}{2^{n\alpha-1}} + \mathcal{O}((2^n)^{1-2\alpha}) \right) \\
&\quad \times \left(\zeta(2\beta, 1) - \frac{1}{2} + (\zeta(\beta, 1) - \frac{1}{2}) \frac{\zeta(\beta, 1/2) + \zeta(\beta, 1)}{2^{n\beta-1}} + \mathcal{O}((2^n)^{1-2\beta}) \right) \\
&\quad - 4C^2 \left(\zeta(2\alpha, 1) - \frac{1}{2} - \zeta(2\alpha, \Lambda + 2) + (\zeta(\alpha, 1) - \frac{1}{2} - \zeta(\alpha, \Lambda + 2)) \frac{\zeta(\alpha, 1/2) + \zeta(\alpha, 1)}{2^{n\alpha-1}} + \mathcal{O}(\Lambda(2^n)^{-2\alpha}) \right) \\
&\quad \times \left(\zeta(2\beta, 1) - \frac{1}{2} - \zeta(2\beta, \Lambda + 2) + (\zeta(\beta, 1) - \frac{1}{2} - \zeta(\beta, \Lambda + 2)) \frac{\zeta(\beta, 1/2) + \zeta(\beta, 1)}{2^{n\beta-1}} + \mathcal{O}(\Lambda(2^n)^{-2\beta}) \right) \\
&= 4C^2 \left(\left(\zeta(2\alpha, \Lambda + 2) + \zeta(\alpha, \Lambda + 2) \frac{\zeta(\alpha, 1/2) + \zeta(\alpha, 1)}{2^{n\alpha-1}} \right) \left(\zeta(2\beta, 1) - \frac{1}{2} + (\zeta(\beta, 1) - \frac{1}{2}) \frac{\zeta(\beta, 1/2) + \zeta(\beta, 1)}{2^{n\beta-1}} \right) \right. \\
&\quad \left. + \left(\zeta(2\beta, \Lambda + 2) + \zeta(\beta, \Lambda + 2) \frac{\zeta(\beta, 1/2) + \zeta(\beta, 1)}{2^{n\beta-1}} \right) \left(\zeta(2\alpha, 1) - \frac{1}{2} + (\zeta(\alpha, 1) - \frac{1}{2}) \frac{\zeta(\alpha, 1/2) + \zeta(\alpha, 1)}{2^{n\alpha-1}} \right) \right. \\
&\quad \left. + \left(\zeta(2\alpha, \Lambda + 2) + \zeta(\alpha, \Lambda + 2) \frac{\zeta(\alpha, 1/2) + \zeta(\alpha, 1)}{2^{n\alpha-1}} \right) \left(\zeta(2\beta, \Lambda + 2) + \zeta(\beta, \Lambda + 2) \frac{\zeta(\beta, 1/2) + \zeta(\beta, 1)}{2^{n\beta-1}} \right) \right) \\
&\quad + \mathcal{O}((2^n)^{1-2\alpha}, (2^n)^{1-2\beta}), \tag{B31}
\end{aligned}$$

where we have used that $\zeta(s, a) = \mathcal{O}(a^{1-s})$ for large a [112]. Notably, this bound does not increase with system size.

Since we must have that $2^n > 2\Lambda$, for large Λ the bound behaves as

$$\sum_{(p,q) \in I_{\text{disc}}} |\hat{f}_{pq}|^2 \leq \mathcal{O}(\Lambda^{1-2\alpha}) + \mathcal{O}(\Lambda^{1-2\beta}) + \mathcal{O}((2^n)^{1-2\alpha}, (2^n)^{1-2\beta}). \quad (\text{B32})$$

This is the result presented in the main text.

Appendix C: Error bounds from cosine transforms

The error bounds for an MPS approximation we presented in the main text crucially depend on how quickly the Fourier coefficients of the function $F(x, y)$ decay. Since the decay of the Fourier coefficients of a function can be related to the smoothness of the function [77], any discontinuous jumps could decrease the efficiency of an MPS approximation. When we wrote down the Fourier series of $F(x, y)$ in Eq. (7), we implicitly extended the function periodically from $(x, y) \in [0, 1]^2$ to $(x, y) \in \mathbb{R}^2$, which can create discontinuous jumps at the boundary of the original input domain $[0, 1]^2$. Because of this, one usually uses cosine transforms instead of Fourier transforms in image processing, which corresponds to first mirroring the original function $F(x, y)$ about the origin to get a larger input domain $[-1, 1]$, and then periodically extending this function with the larger input domain by doing a Fourier transform. This way, there are no more discontinuous jumps at the boundary, only discontinuities in the derivatives remain.

There are several different cosine transforms, which can be related to Fourier transforms of input data with a larger size and a certain symmetry. We will review this connection for the type I and type II discrete cosine transforms here, and show what changes in the error bounds.

1. Type-I DCT

First, let us consider the discrete cosine transform of type I (DCT-I). The forward DCT-I of a matrix f_{ab} , $a, b \in \{0, 1, \dots, 2^n - 1\}$ produces coefficients \hat{f}_{pq} , $p, q \in \{0, 1, \dots, 2^n - 1\}$, which are defined as

$$\begin{aligned} \hat{f}_{pq} &= \frac{1}{(2^n - 1)^2} \\ &\times \sum_{a,b=0}^{2^n - 1} \frac{f_{ab} \cos\left(\frac{\pi pa}{2^n - 1}\right) \cos\left(\frac{\pi qb}{2^n - 1}\right)}{(1 + \delta_{a,0} + \delta_{a,2^n - 1})(1 + \delta_{a,0} + \delta_{a,2^n - 1})} \quad (\text{C1}) \\ &= \frac{1}{(2(2^n - 1))^2} \sum_{a,b=-2^n + 1}^{2^n - 2} h_{ab} e^{-i\frac{2\pi pa}{2(2^n - 1)}} e^{-i\frac{2\pi qb}{2(2^n - 1)}} \end{aligned}$$

defining a new matrix of larger dimension $h_{ab} = f_{|a|,|b|}$ for $a, b \in \{-2^n + 1, -2^n + 2, \dots, 2^n - 2\}$. The inverse

transform is defined as

$$\begin{aligned} f_{ab} &= \sum_{p,q=0}^{2^n - 1} \hat{f}_{pq} (2 - \delta_{p,0} - \delta_{p,2^n - 1})(2 - \delta_{q,0} - \delta_{q,2^n - 1}) \\ &\times \cos\left(\frac{\pi pa}{2^n - 1}\right) \cos\left(\frac{\pi qb}{2^n - 1}\right) \quad (\text{C2}) \\ &= \sum_{p,q=-2^n + 1}^{2^n - 2} \hat{h}_{pq} e^{i\frac{2\pi pa}{2(2^n - 1)}} e^{i\frac{2\pi qb}{2(2^n - 1)}}, \end{aligned}$$

defining a new matrix of Fourier coefficients $\hat{h}_{pq} = \hat{f}_{|p|,|q|}$ for $p, q \in \{-2^n + 1, -2^n + 2, \dots, 2^n - 2\}$. From this we can see that the DCT-I of the $2^n \times 2^n$ matrix f_{ab} is equivalent to the DFT of the $2(2^n - 1) \times 2(2^n - 1)$ matrix h_{ab} , the coefficients of which are just f_{ab} arranged to have a mirror symmetry about the origin.

This can be extended to the cosine series of the function $F(x, y)$ with continuous arguments $(x, y) \in [0, 1]^2$; the coefficients of the cosine series are given by

$$\begin{aligned} \hat{F}(k, \ell) &= \int_0^1 dx \int_0^1 dy \frac{F(x, y) \cos(\pi kx) \cos(\pi \ell y)}{(1 + \delta_{k,0})(1 + \delta_{\ell,0})} \\ &= \frac{1}{2^2} \int_{-1}^1 dx \int_{-1}^1 dy H(x, y) e^{-i2\pi \frac{k}{2}x} e^{-i2\pi \frac{\ell}{2}y}, \quad (\text{C3}) \end{aligned}$$

defining the new function $H(x, y) = F(|x|, |y|)$ on the extended domain $(x, y) \in [-1, 1]^2$; the cosine series is

$$\begin{aligned} F(x, y) &= \sum_{p,q=0}^{\infty} \hat{F}(k, \ell) (2 - \delta_{k,0})(2 - \delta_{\ell,0}) \\ &\times \cos(\pi kx) \cos(\pi \ell y) \quad (\text{C4}) \\ &= \sum_{p,q \in \mathbb{Z}} \hat{H}(k, \ell) e^{i2\pi \frac{k}{2}x} e^{i2\pi \frac{\ell}{2}y} \end{aligned}$$

defining the Fourier coefficients $\hat{H}(k, \ell) = \hat{F}(|k|, |\ell|)$ for $k, \ell \in \mathbb{Z}$. Hence, the cosine series of the function $F(x, y)$ defined on $(x, y) \in [0, 1]^2$ is equivalent to the Fourier series of the function $H(x, y)$ defined on $(x, y) \in [-1, 1]^2$, which is just the function F mirrored about the origin. The advantage here is that if $F(x, y)$ was continuous on $(x, y) \in [0, 1]^2$, then the periodically extended function $H(x, y)$ is continuous for all $(x, y) \in \mathbb{R}^2$ —in particular, there are no discontinuities at the boundary of the original domain. This should lead to a quicker decay of the Fourier coefficients $\hat{H}(k, \ell)$ compared to $\hat{F}(k, \ell)$.

Sampling $F(x, y)$ on the $2^n \times 2^n$ grid $(x, y) = (\frac{a}{2^n - 1}, \frac{b}{2^n - 1})$, $a, b \in \{0, 1, \dots, 2^n - 1\}$, and relating the coefficients $\hat{F}(k, \ell)$ to the coefficients of the DCT-I of $f_{ab} = (\frac{a}{2^n - 1}, \frac{b}{2^n - 1})$ is equivalent to sampling the function $H(x, y)$ on the $2(2^n - 1) \times 2(2^n - 1)$ grid $(x, y) = (\frac{a}{2^n - 1}, \frac{b}{2^n - 1})$, $a, b \in \{-2^n + 1, -2^n + 2, \dots, 2^n - 2\}$, and relating the coefficients of the Fourier series to the DFT. This is the case considered in the main text, and using Eq. (9) in this context yields

$$\hat{h}_{pq} = \sum_{i,j \in \mathbb{Z}} \hat{H}(p + i2(2^n - 1), q + j2(2^n - 1)) \quad (\text{C5})$$

for $p, q \in \{-2^n + 1, -2^n + 2, \dots, 2^n - 2\}$.

With the representation as a Fourier transform, we can use the same derivation for an MPS representation as in App. A. A difference arises in the calculation of the error bounds, as now the Fourier transform includes more frequencies, i.e., $p, q \in \{-2^n + 1, -2^n + 2, \dots, 2^n - 2\}$ then there are pixels, i.e., $a, b \in \{0, 1, \dots, 2^n - 1\}$. Still, we can proceed similarly as in the main text. For notational convenience, we define the three index sets $I_{\text{all}} = \{-2^n + 1, -2^n + 2, \dots, 2^n - 2\}^2$, containing all possible frequency pairs; $I_{\text{appr}} = \{-\Lambda, -\Lambda + 1, \dots, \Lambda\}^2$, containing all frequency pairs retained in the approximation; and $I_{\text{disc}} = I_{\text{all}} \setminus I_{\text{appr}}$, containing all frequency pairs discarded in the approximation. Using this, we can express f_{ab} as

$$\begin{aligned} f_{ab} &= \sum_{(p,q) \in I_{\text{all}}} \hat{h}_{pq} e^{i \frac{2\pi p a}{2(2^n - 1)}} e^{i \frac{2\pi q b}{2(2^n - 1)}} \\ &= 2(2^n - 1)(U \hat{h} U^T)_{ab}, \end{aligned} \quad (\text{C6})$$

where in contrast to the main text \hat{h}_{pq} is a $2(2^n - 1) \times 2(2^n - 1)$ matrix and $U_{ap} = \frac{1}{\sqrt{2(2^n - 1)}} e^{i \frac{2\pi p a}{2(2^n - 1)}}$ is now a $2^n \times 2(2^n - 1)$ isometric matrix instead of a unitary one.⁸ As before, we obtain the approximation g_{ab} to f_{ab} by retaining only Fourier modes up to a cutoff Λ , which gives

$$\begin{aligned} g_{ab} &= \sum_{(p,q) \in I_{\text{appr}}} \hat{f}_{pq} e^{i \frac{2\pi p a}{2(2^n - 1)}} e^{i \frac{2\pi q b}{2(2^n - 1)}} \\ &= 2(2^n - 1)(U \hat{g} U^T)_{ab}, \end{aligned} \quad (\text{C7})$$

where \hat{g} is the matrix of the truncated Fourier coefficients, i.e., for $|p| \leq \Lambda$ and $|q| \leq \Lambda$ we have $\hat{g}_{pq} = \hat{h}_{pq}$ but if either $|p| > \Lambda$ or $|q| > \Lambda$ then $\hat{g}_{pq} = 0$. The expression for the approximation error in Eq. (18) still holds, but now expressing it in terms of Fourier coefficients requires a bit of caution; we have

$$\begin{aligned} \|f - g\|_F &= \\ &= 2(2^n - 1) \|U(\hat{h} - \hat{g})U^T\|_F \\ &= 2(2^n - 1) \|(U \otimes U) \text{vec}(\hat{h} - \hat{g})\|_2 \\ &= 2(2^n - 1) (\text{vec}(\hat{h} - \hat{g})^\dagger (U^\dagger \otimes U^\dagger) \\ &\quad \cdot (U \otimes U) \text{vec}(\hat{h} - \hat{g}))^{\frac{1}{2}} \\ &= 2(2^n - 1) (\text{vec}(\hat{h} - \hat{g})^\dagger (P \otimes P) \text{vec}(\hat{h} - \hat{g}))^{\frac{1}{2}} \\ &\leq 2(2^n - 1) (\text{vec}(\hat{h} - \hat{g})^\dagger (\mathbb{1} \otimes \mathbb{1}) \text{vec}(\hat{h} - \hat{g}))^{\frac{1}{2}} \\ &= 2(2^n - 1) \|\hat{h} - \hat{g}\|_F, \end{aligned} \quad (\text{C8})$$

where $\text{vec}(\hat{h} - \hat{g})$ denotes the vectorized version of the

⁸ An isometric matrix U is one for which $UU^\dagger = \mathbb{1}$ but $U^\dagger U = P \neq \mathbb{1}$, with $P = P^2$ a projector matrix.

matrix $\hat{h} - \hat{g}$, and

$$\begin{aligned} \|g\|_F &= 2(2^n - 1) \|U \hat{g} U^T\|_F \\ &= 2(2^n - 1) \sqrt{\text{Tr}(U^* \hat{g}^\dagger U^\dagger U \hat{g} U^T)} \\ &= 2(2^n - 1) \sqrt{\text{Tr}(P^* \hat{g}^\dagger P \hat{g})}; \end{aligned} \quad (\text{C9})$$

thus Eq. (19) becomes

$$\| |f\rangle - |g\rangle \|_2 \leq \frac{2\|f - g\|_F}{\|g\|_F} \leq \frac{2\|\hat{h} - \hat{g}\|_F}{\sqrt{\text{Tr}(P^* \hat{g}^\dagger P \hat{g})}}. \quad (\text{C10})$$

For $\|\hat{h} - \hat{g}\|_F = \sqrt{\sum_{(p,q) \in I_{\text{disc}}} |\hat{h}_{pq}|^2}$ we can reuse the results from App. B: if the coefficients of the cosine series $\hat{F}(k, \ell)$ decay exponentially or algebraically, then also the Fourier coefficients $\hat{H}(k, \ell)$ decay this way, however, we must substitute $2^n \rightarrow 2(2^n - 1)$ as there are now more Fourier coefficients. Still, this leads to an approximation error independent of the size of the image. The factor $1/\sqrt{\text{Tr}(P^* \hat{g}^\dagger P \hat{g})}$ generically does not introduce an asymptotic scaling. Since \hat{g} is a $2(2^n - 1) \times 2(2^n - 1)$ matrix where only the central $(2\Lambda + 1) \times (2\Lambda + 1)$ square is nonzero, the increasing matrix dimension of $P = U^\dagger U$ has no effect on the result of $\text{Tr}(P^* \hat{g}^\dagger P \hat{g})$. The nonzero values of \hat{g} are the values of $\hat{H}(k, \ell)$ up the cutoff Λ , plus corrections which are exponentially or algebraically small in the number of pixels, depending on the decay of $|\hat{H}(k, \ell)|$ —see also Eqs. (B5) and (B19). So as long as not all coefficients of the Fourier series within the cutoff are zero, $\text{Tr}(P^* \hat{g}^\dagger P \hat{g})$ will not become zero as the number of pixels is increased. Its inverse can thus not diverge, and hence not change the dominant term in the asymptotic scaling.

2. Type-II DCT

Now we consider the type-II discrete cosine transform (DCT-II), which is more common than the DCT-I and for example used in the JPEG algorithm for image compression. The forward DCT-II of a matrix f_{ab} , $a, b \in \{0, 1, \dots, 2^n - 1\}$ produces coefficients \hat{f}_{pq} , $p, q \in \{0, 1, \dots, 2^n - 1\}$, which are defined as

$$\begin{aligned} \hat{f}_{pq} &= \frac{1}{(2^n)^2} \sum_{a,b=0}^{2^n-1} f_{ab} \\ &\quad \times \cos\left(\frac{\pi p}{2^n} \left(a + \frac{1}{2}\right)\right) \cos\left(\frac{\pi q}{2^n} \left(b + \frac{1}{2}\right)\right) \\ &= \frac{1}{(2^{n+1})^2} \sum_{a,b=-2^n}^{2^n-1} h_{ab} e^{-i \frac{2\pi p}{2^{n+1}} \left(a + \frac{1}{2}\right)} e^{-i \frac{2\pi q}{2^{n+1}} \left(b + \frac{1}{2}\right)} \end{aligned} \quad (\text{C11})$$

defining a new matrix of larger dimension $h_{ab} = f_{|a+\frac{1}{2}|-\frac{1}{2}, |b+\frac{1}{2}|-\frac{1}{2}}$ for $a, b \in \{-2^n, -2^n + 1, \dots, 2^n - 1\}$.

The inverse transform is defined as

$$\begin{aligned}
f_{ab} &= \sum_{p,q=0}^{2^n-1} \hat{f}_{pq} (2 - \delta_{p,0})(2 - \delta_{q,0}) \\
&\quad \times \cos\left(\frac{\pi p}{2^n}\left(a + \frac{1}{2}\right)\right) \cos\left(\frac{\pi q}{2^n}\left(b + \frac{1}{2}\right)\right) \quad (\text{C12}) \\
&= \sum_{p,q=-2^n}^{2^n-1} \hat{h}_{pq} e^{i\frac{2\pi p}{2^{n+1}}\left(a+\frac{1}{2}\right)} e^{i\frac{2\pi q}{2^{n+1}}\left(b+\frac{1}{2}\right)},
\end{aligned}$$

defining a new $2^n \times 2^n$ matrix of Fourier coefficients \hat{h}_{pq} with $\hat{h}_{pq} = \hat{f}_{|p|,|q|}$ for $p, q \in \{-2^n + 1, -2^n + 2, \dots, 2^n - 1\}$ and $\hat{h}_{pq} = 0$ if either $p = -2^n$ or $q = -2^n$.⁹ The DCT-II of the $2^n \times 2^n$ matrix f_{ab} is thus equivalent to the quarter-wave DFT of the $2^{n+1} \times 2^{n+1}$ matrix h_{ab} , where each $2^n \times 2^n$ quadrant of h_{ab} is a copy of f_{ab} , mirrored such that the matrix is point-symmetric about its center, i.e., such that $h_{ab} = h_{-a-1, b} = h_{a, -b-1}$ for $a, b \in \{-2^n, -2^n + 1, \dots, 2^n - 1\}$.

The coefficients of the cosine series of $F(x, y)$, $(x, y) \in [0, 1]^2$, are given by

$$\begin{aligned}
\hat{F}(k, \ell) &= \int_0^1 dx \int_0^1 dy \frac{F(x, y) \cos(\pi kx) \cos(\pi \ell y)}{(1 + \delta_{k,0})(1 + \delta_{\ell,0})} \\
&= \frac{1}{2^2} \int_{-1}^1 dx \int_{-1}^1 dy H(x, y) e^{-i2\pi \frac{k}{2}x} e^{-i2\pi \frac{\ell}{2}y}, \quad (\text{C13})
\end{aligned}$$

defining the new function $H(x, y) = F(|x|, |y|)$ on the extended domain $(x, y) \in [-1, 1]^2$; the cosine series is

$$\begin{aligned}
F(x, y) &= \sum_{p,q=0}^{\infty} \hat{F}(k, \ell) (2 - \delta_{k,0})(2 - \delta_{\ell,0}) \\
&\quad \times \cos(\pi kx) \cos(\pi \ell y) \quad (\text{C14}) \\
&= \sum_{p,q \in \mathbb{Z}} \hat{H}(k, \ell) e^{i2\pi \frac{k}{2}x} e^{i2\pi \frac{\ell}{2}y}
\end{aligned}$$

defining the Fourier coefficients $\hat{H}(k, \ell) = \hat{F}(|k|, |\ell|)$ for

$k, \ell \in \mathbb{Z}$. This yields the same function $H(x, y)$ encountered for the DCT-I, however, instead of sampling $F(x, y)$ on the $2^n \times 2^n$ grid with coordinates $(x, y) = (\frac{a}{2^n-1}, \frac{b}{2^n-1})$, $a, b \in \{0, 1, \dots, 2^n - 1\}$, we sample it on the $2^n \times 2^n$ grid with coordinates $(x, y) = (\frac{a+1/2}{2^n}, \frac{b+1/2}{2^n})$, $a, b \in \{0, 1, \dots, 2^n - 1\}$. Relating the coefficients $\hat{F}(k, \ell)$ of the cosine series to the coefficients of the DCT-II is equivalent to sampling the function $H(x, y)$ on the $2^{n+1} \times 2^{n+1}$ grid $(x, y) = (\frac{a+1/2}{2^n}, \frac{b+1/2}{2^n})$ with $a, b \in \{-2^n, -2^n + 1, \dots, 2^n - 1\}$ and relating the coefficients of the Fourier series to the quarter-wave DFT. Using $e^{i2\pi(k+j2^{n+1})(a+\frac{1}{2})/2^{n+1}} = (-1)^j e^{i2\pi k(a+\frac{1}{2})/2^{n+1}}$ yields a relation similar to Eq. (9):

$$\hat{h}_{pq} = \sum_{i,j \in \mathbb{Z}} (-1)^{i+j} \hat{H}(p + i2N, q + j2N) \quad (\text{C15})$$

for $p, q \in \{-N, -N + 1, \dots, N - 1\}$.

Similarly to the case for the DCT-I, we can now reuse the results from the main text under certain substitutions. The MPS construction follows from the representation of the DCT-II as a quarter-wave DFT, where the extra phase due to the shift of the indices a and b by $1/2$ can be absorbed in the DFT coefficients. The bounds on the approximation error when $\hat{F}(k, \ell)$ decays exponentially or algebraically can be reused if one substitutes $2^n \rightarrow 2^{n+1}$, as then also $\hat{H}(k, \ell)$ decays in the same way, however there are now twice as many Fourier coefficients. The additional phases in Eq. (C15) compared to Eq. (9) do not play a role, as only the absolute value is relevant.

-
- [1] J. Biamonte, P. Wittek, N. Pancotti, P. Rebentrost, N. Wiebe, and S. Lloyd, Quantum machine learning, *Nature* **549**, 195 (2017), arXiv:1611.09347 [quant-ph].
- [2] M. Schuld and F. Petruccione, *Supervised Learning with Quantum Computers*, edited by R. Laflamme, G. Lenhart, D. Lidar, A. Rauschenbeutel, R. Renner, M. Schlosshauer, Y. S. Weinstein, and H. M. Wiseman, Quantum Science and Technology, Vol. 2 (Springer, Cham, 2018).

- [3] Y. Liu, S. Arunachalam, and K. Temme, A rigorous and robust quantum speed-up in supervised machine learning, *Nature Physics* **17**, 1013 (2021), arXiv:2010.02174 [quant-ph].
- [4] R. Sweke, J.-P. Seifert, D. Hangleiter, and J. Eisert, On the quantum versus classical learnability of discrete distributions, *Quantum* **5**, 417 (2021), arXiv:2007.14451 [quant-ph].
- [5] H.-Y. Huang, M. Broughton, M. Mohseni, R. Babbush, S. Boixo, H. Neven, and J. R. McClean, Power of data in quantum machine learning, *Nature Communications* **12**, 2631 (2021), arXiv:2011.01938 [quant-ph].
- [6] N. Pirnay, R. Sweke, J. Eisert, and J.-P. Seifert, Superpolynomial quantum-classical separation for density modeling, *Physical Review A* **107**, 042416 (2023),

⁹ The condition $\hat{g}_{pq} = 0$ for $p = -2^n$ or $q = -2^n$ follows from the symmetry $g_{ab} = g_{-a-1, b} = g_{a, -b-1}$ of the inputs g_{ab} . This can be seen by explicitly calculating $\hat{g}_{-2^n, q}$ or $\hat{g}_{p, -2^n}$.

- arXiv:2210.14936 [quant-ph].
- [7] C. Gyurik and V. Dunjko, Exponential separations between classical and quantum learners, *arXiv preprint (2023)*, arXiv:2306.16028 [quant-ph].
 - [8] N. Wiebe, D. Braun, and S. Lloyd, Quantum algorithm for data fitting, *Physical Review Letters* **109**, 050505 (2012), arXiv:1204.5242 [quant-ph].
 - [9] I. Cong, S. Choi, and M. D. Lukin, Quantum convolutional neural networks, *Nature Physics* **15**, 1273 (2019), arXiv:1810.03787 [quant-ph].
 - [10] Y.-J. Liu, A. Smith, M. Knap, and F. Pollmann, Model-independent learning of quantum phases of matter with quantum convolutional neural networks, *Physical Review Letters* **130**, 220603 (2023), arXiv:2211.11786 [quant-ph].
 - [11] E. Lake, S. Balasubramanian, and S. Choi, Exact quantum algorithms for quantum phase recognition: Renormalization group and error correction, *arXiv preprint (2023)*, arXiv:2211.09803 [quant-ph].
 - [12] P. Reberntrost, M. Mohseni, and S. Lloyd, Quantum support vector machine for big data classification, *Physical Review Letters* **113**, 130503 (2014), arXiv:1307.0471 [quant-ph].
 - [13] V. Havlíček, A. D. Córcoles, K. Temme, A. W. Harrow, A. Kandala, J. M. Chow, and J. M. Gambetta, Supervised learning with quantum-enhanced feature spaces, *Nature* **567**, 209 (2019), arXiv:1804.11326 [quant-ph].
 - [14] M. Schuld, R. Sweke, and J. J. Meyer, Effect of data encoding on the expressive power of variational quantum-machine-learning models, *Physical Review A* **103**, 032430 (2021), arXiv:2008.08605 [quant-ph].
 - [15] M. Plesch and Č. Brukner, Quantum-state preparation with universal gate decompositions, *Physical Review A* **83**, 032302 (2011), arXiv:1003.5760 [quant-ph].
 - [16] R. Iten, R. Colbeck, I. Kukuljan, J. Home, and M. Christandl, Quantum circuits for isometries, *Physical Review A* **93**, 032318 (2016), arXiv:1501.06911 [quant-ph].
 - [17] M. G. Amankwah, D. Camps, E. W. Bethel, R. V. Beeumen, and T. Perciano, Quantum pixel representations and compression for N -dimensional images, *Scientific Reports* **12**, 7712 (2022), arXiv:2110.04405 [quant-ph].
 - [18] S. Aaronson, Read the fine print, *Nature Physics* **11**, 291 (2015).
 - [19] M. Moosa, T. W. Watts, Y. Chen, A. Sarma, and P. L. McMahon, Linear-depth quantum circuits for loading Fourier approximations of arbitrary functions, *Quantum Science and Technology* **9**, 015002 (2023), arXiv:2302.03888 [quant-ph].
 - [20] J. J. García-Ripoll, Quantum-inspired algorithms for multivariate analysis: from interpolation to partial differential equations, *Quantum* **5**, 431 (2021), arXiv:1909.06619 [quant-ph].
 - [21] A. Holmes and A. Y. Matsuura, Efficient quantum circuits for accurate state preparation of smooth, differentiable functions, in *2020 IEEE International Conference on Quantum Computing and Engineering (QCE)* (2020) pp. 169–179, arXiv:2005.04351 [quant-ph].
 - [22] R. Dilip, Y.-J. Liu, A. Smith, and F. Pollmann, Data compression for quantum machine learning, *Physical Review Research* **4**, 043007 (2022), arXiv:2204.11170 [quant-ph].
 - [23] J. Iaconis and S. Johri, Tensor network based efficient quantum data loading of images, *arXiv preprint (2023)*, arXiv:2310.05897 [quant-ph].
 - [24] C. Schön, E. Solano, F. Verstraete, J. I. Cirac, and M. M. Wolf, Sequential generation of entangled multi-qubit states, *Physical Review Letters* **95**, 110503 (2005), arXiv:quant-ph/0501096 [quant-ph].
 - [25] C. Schön, K. Hammerer, M. M. Wolf, J. I. Cirac, and E. Solano, Sequential generation of matrix-product states in cavity QED, *Physical Review A* **75**, 032311 (2007), arXiv:quant-ph/0612101 [quant-ph].
 - [26] M. Lubasch, J. Joo, P. Moinier, M. Kiffner, and D. Jaksch, Variational quantum algorithms for nonlinear problems, *Physical Review A* **101**, 010301 (2020), arXiv:1907.09032 [quant-ph].
 - [27] A. Smith, B. Jobst, A. G. Green, and F. Pollmann, Crossing a topological phase transition with a quantum computer, *Physical Review Research* **4**, L022020 (2022), arXiv:1910.05351 [cond-mat.str-el].
 - [28] S.-H. Lin, R. Dilip, A. G. Green, A. Smith, and F. Pollmann, Real- and imaginary-time evolution with compressed quantum circuits, *PRX Quantum* **2**, 010342 (2021), arXiv:2008.10322 [quant-ph].
 - [29] F. Barratt, J. Dborin, M. Bal, V. Stojevic, F. Pollmann, and A. G. Green, Parallel quantum simulation of large systems on small NISQ computers, *npj Quantum Information* **7**, 79 (2021), arXiv:2003.12087 [quant-ph].
 - [30] D. K. Park, F. Petruccione, and J.-K. K. Rhee, Circuit-based quantum random access memory for classical data, *Scientific Reports* **9**, 3949 (2019), arXiv:1901.02362 [quant-ph].
 - [31] H. Wang, S. Ashhab, and F. Nori, Efficient quantum algorithm for preparing molecular-system-like states on a quantum computer, *Physical Review A* **79**, 042335 (2009), arXiv:0902.1419 [quant-ph].
 - [32] O. D. Matteo, V. Gheorghiu, and M. Mosca, Fault-tolerant resource estimation of quantum random-access memories, *IEEE Transactions on Quantum Engineering* **1**, 1 (2020), arXiv:1902.01329 [quant-ph].
 - [33] S. Ashhab, Quantum state preparation protocol for encoding classical data into the amplitudes of a quantum information processing register's wave function, *Physical Review Research* **4**, 013091 (2022), arXiv:2107.14127 [quant-ph].
 - [34] J. P. Gaebler, C. H. Baldwin, S. A. Moses, J. M. Dreiling, C. Figgatt, M. Foss-Feig, D. Hayes, and J. M. Pino, Suppression of midcircuit measurement crosstalk errors with micromotion, *Physical Review A* **104**, 062440 (2021), arXiv:2108.10932 [quant-ph].
 - [35] K. Rudinger, G. J. Ribeill, L. C. Govia, M. Ware, E. Nielsen, K. Young, T. A. Ohki, R. Blume-Kohout, and T. Proctor, Characterizing midcircuit measurements on a superconducting qubit using gate set tomography, *Physical Review Applied* **17**, 014014 (2022), arXiv:2103.03008 [quant-ph].
 - [36] T. M. Graham, L. Phuttitarn, R. Chinnarasu, Y. Song, C. Poole, K. Jooya, J. Scott, A. Scott, P. Eichler, and M. Saffman, Mid-circuit measurements on a neutral atom quantum processor, *arXiv preprint (2023)*, arXiv:2303.10051 [quant-ph].
 - [37] M. Lubasch, P. Moinier, and D. Jaksch, Multigrid renormalization, *Journal of Computational Physics* **372**, 587 (2018), arXiv:1802.07259 [physics.comp-ph].
 - [38] N. Gourianov, M. Lubasch, S. Dolgov, Q. Y. van den Berg, H. Babae, P. Givi, M. Kiffner, and D. Jaksch, A quantum-inspired approach to exploit turbulence structures, *Nature Computational Science* **2**, 30 (2022),

- arXiv:2106.05782 [physics.flu-dyn].
- [39] Y. Núñez Fernández, M. Jeannin, P. T. Dumitrescu, T. Kloss, J. Kaye, O. Parcollet, and X. Waintal, Learning Feynman diagrams with tensor trains, *Physical Review X* **12**, 041018 (2022), arXiv:2207.06135 [cond-mat.str-el].
- [40] M. K. Ritter, Y. Núñez Fernández, M. Wallerberger, J. von Delft, H. Shinaoka, and X. Waintal, Quantics tensor cross interpolation for high-resolution, parsimonious representations of multivariate functions in physics and beyond, arXiv preprint (2023), arXiv:2303.11819 [physics.comp-ph].
- [41] J. Howard, *Imagenette* (2019), <https://github.com/fastai/imagenette>.
- [42] J. Deng, W. Dong, R. Socher, L.-J. Li, K. Li, and L. Fei-Fei, ImageNet: A large-scale hierarchical image database, in *2009 IEEE Conference on Computer Vision and Pattern Recognition* (2009) pp. 248–255, <https://www.image-net.org>.
- [43] H. Xiao, K. Rasul, and R. Vollgraf, Fashion-MNIST: a novel image dataset for benchmarking machine learning algorithms (2017), <https://github.com/zalando-research/fashion-mnist>, arXiv:1708.07747 [cs.LG].
- [44] J. I. Latorre, Image compression and entanglement, arXiv preprint (2005), arXiv:quant-ph/0510031 [quant-ph].
- [45] P. Q. Le, F. Dong, and K. Hirota, A flexible representation of quantum images for polynomial preparation, image compression, and processing operations, *Quantum Information Processing* **10**, 63 (2011).
- [46] P. Q. Le, A. M. Ilyasu, F. Dong, and K. Hirota, A flexible representation and invertible transformations for images on quantum computers, in *New Advances in Intelligent Signal Processing*, Vol. 372, edited by A. E. Ruano and A. R. Várkonyi-Kóczy (Springer Berlin Heidelberg, Berlin, Heidelberg, 2011) pp. 179–202.
- [47] R. A. Khan, An improved flexible representation of quantum images, *Quantum Information Processing* **18**, 201 (2019).
- [48] Y. Zhang, K. Lu, Y. Gao, and M. Wang, NEQR: a novel enhanced quantum representation of digital images, *Quantum Information Processing* **12**, 2833 (2013).
- [49] N. Jiang and L. Wang, Quantum image scaling using nearest neighbor interpolation, *Quantum Information Processing* **14**, 1559 (2014).
- [50] B. Sun, P. Q. Le, A. M. Ilyasu, F. Yan, J. A. Garcia, F. Dong, and K. Hirota, A multi-channel representation for images on quantum computers using the RGB α color space, in *2011 IEEE 7th International Symposium on Intelligent Signal Processing* (2011) pp. 1–6.
- [51] B. Sun, A. M. Ilyasu, F. Yan, F. Dong, and K. Hirota, An RGB multi-channel representation for images on quantum computers, *Journal of Advanced Computational Intelligence and Intelligent Informatics* **17**, 404 (2013).
- [52] J. Sang, S. Wang, and Q. Li, A novel quantum representation of color digital images, *Quantum Information Processing* **16**, 42 (2016).
- [53] J. Su, X. Guo, C. Liu, S. Lu, and L. Li, An improved novel quantum image representation and its experimental test on IBM quantum experience, *Scientific Reports* **11**, 13879 (2021).
- [54] R. Schützhold, Pattern recognition on a quantum computer, *Physical Review A* **67**, 062311 (2003), arXiv:quant-ph/0208063 [quant-ph].
- [55] Y. Zhang, K. Lu, and Y. Gao, QSobel: A novel quantum image edge extraction algorithm, *Science China Information Sciences* **58**, 1 (2015).
- [56] P. Q. Le, A. M. Ilyasu, F. Dong, and K. Hirota, Efficient color transformations on quantum images, *Journal of Advanced Computational Intelligence and Intelligent Informatics* **15**, 698 (2011).
- [57] Y. Zhang, K. Lu, K. Xu, Y. Gao, and R. Wilson, Local feature point extraction for quantum images, *Quantum Information Processing* **14**, 1573 (2015).
- [58] N. Jiang, J. Wang, and Y. Mu, Quantum image scaling up based on nearest-neighbor interpolation with integer scaling ratio, *Quantum Information Processing* **14**, 4001 (2015).
- [59] D. N. Page, Average entropy of a subsystem, *Physical Review Letters* **71**, 1291 (1993), arXiv:gr-qc/9305007 [gr-qc].
- [60] J. Sietsma and R. J. Dow, Creating artificial neural networks that generalize, *Neural Networks* **4**, 67 (1991).
- [61] C. M. Bishop, Training with noise is equivalent to Tikhonov regularization, *Neural Computation* **7**, 108 (1995).
- [62] G. An, The effects of adding noise during backpropagation training on a generalization performance, *Neural Computation* **8**, 643 (1996).
- [63] F. Verstraete and J. I. Cirac, Matrix product states represent ground states faithfully, *Physical Review B* **73**, 094423 (2006), arXiv:cond-mat/0505140 [cond-mat.str-el].
- [64] N. Schuch, M. M. Wolf, F. Verstraete, and J. I. Cirac, Entropy scaling and simulability by matrix product states, *Physical Review Letters* **100**, 030504 (2008), arXiv:0705.0292 [quant-ph].
- [65] M. B. Hastings, An area law for one-dimensional quantum systems, *Journal of Statistical Mechanics: Theory and Experiment*, P08024 (2007), arXiv:0705.2024 [quant-ph].
- [66] D. Gottesman and M. B. Hastings, Entanglement versus gap for one-dimensional spin systems, *New Journal of Physics* **12**, 025002 (2010), arXiv:0901.1108 [quant-ph].
- [67] J. Eisert, M. Cramer, and M. B. Plenio, Colloquium: Area laws for the entanglement entropy, *Reviews of Modern Physics* **82**, 277 (2010), arXiv:0808.3773 [quant-ph].
- [68] U. Schollwöck, The density-matrix renormalization group in the age of matrix product states, *Annals of Physics* **326**, 96 (2011), arXiv:1008.3477 [cond-mat.str-el].
- [69] M. Fannes, B. Nachtergaele, and R. F. Werner, Finitely correlated states on quantum spin chains, *Communications in Mathematical Physics* **144**, 443 (1992).
- [70] J. I. Cirac, D. Pérez-García, N. Schuch, and F. Verstraete, Matrix product states and projected entangled pair states: Concepts, symmetries, theorems, *Reviews of Modern Physics* **93** (2021), arXiv:2011.12127 [quant-ph].
- [71] B. N. Khoromskij, $O(d \log N)$ -quantics approximation of N - d tensors in high-dimensional numerical modeling, *Constructive Approximation* **34**, 257 (2011).
- [72] I. V. Oseledets, Approximation of $2^d \times 2^d$ matrices using tensor decomposition, *SIAM Journal on Matrix Analysis and Applications* **31**, 2130 (2010).

- [73] I. V. Oseledets, Tensor-train decomposition, *SIAM Journal on Scientific Computing* **33**, 2295 (2011).
- [74] I. V. Oseledets, Constructive representation of functions in low-rank tensor formats, *Constructive Approximation* **37**, 1 (2013).
- [75] B. N. Khoromskij, *Tensor Numerical Methods in Scientific Computing*, edited by O. Scherzer, H. Albrecher, R. H. W. Hoppe, K. Kunisch, H. Niederreiter, and C. Schmeiser, Radon Series on Computational and Applied Mathematics, Vol. 19 (De Gruyter, Berlin, Boston, 2018).
- [76] R.-G. Zhou, Y.-J. Sun, and P. Fan, Quantum image gray-code and bit-plane scrambling, *Quantum Information Processing* **14**, 1717 (2015).
- [77] L. Grafakos, *Classical Fourier Analysis*, 3rd ed., edited by S. Axler and K. Ribet, Graduate Texts in Mathematics, Vol. 249 (Springer, New York, 2014).
- [78] J. Nissilä, Fourier decay of absolutely and Hölder continuous functions with infinitely or finitely many oscillations, *arXiv preprint* (2021), [arXiv:1805.02445](https://arxiv.org/abs/1805.02445) [math.CA].
- [79] S. Herbert, Quantum Monte Carlo integration: The full advantage in minimal circuit depth, *Quantum* **6**, 823 (2022), [arXiv:2105.09100](https://arxiv.org/abs/2105.09100) [quant-ph].
- [80] C. Chamon, A. Hamma, and E. R. Mucciolo, Emergent irreversibility and entanglement spectrum statistics, *Physical Review Letters* **112**, 240501 (2014), [arXiv:1310.2702](https://arxiv.org/abs/1310.2702) [quant-ph].
- [81] D. Shaffer, C. Chamon, A. Hamma, and E. R. Mucciolo, Irreversibility and entanglement spectrum statistics in quantum circuits, *Journal of Statistical Mechanics: Theory and Experiment* **2014**, P12007 (2014), [arXiv:1407.4419](https://arxiv.org/abs/1407.4419) [quant-ph].
- [82] R. Morral Yepes, A. Smith, S. L. Sondhi, and F. Pollmann, Entanglement transitions in unitary circuit games, *arXiv preprint* (2023), [arXiv:2304.12965](https://arxiv.org/abs/2304.12965) [quant-ph].
- [83] N. Astrakhantsev, S.-H. Lin, F. Pollmann, and A. Smith, Time evolution of uniform sequential circuits, *Physical Review Research* **5**, 033187 (2023), [arXiv:2210.03751](https://arxiv.org/abs/2210.03751) [quant-ph].
- [84] A. C. Gilbert, S. Muthukrishnan, and M. Strauss, Improved time bounds for near-optimal sparse Fourier representations, in *Wavelets XI*, Vol. 5914, edited by M. Papadakis, A. F. Laine, and M. A. Unser, International Society for Optics and Photonics (SPIE, 2005) p. 59141A.
- [85] B. Ghazi, H. Hassanieh, P. Indyk, D. Katabi, E. Price, and L. Shi, Sample-optimal average-case sparse Fourier transform in two dimensions, in *2013 51st Annual Allerton Conference on Communication, Control, and Computing (Allerton)* (2013) pp. 1258–1265, [arXiv:1303.1209](https://arxiv.org/abs/1303.1209) [cs.DS].
- [86] A. C. Gilbert, P. Indyk, M. Iwen, and L. Schmidt, Recent developments in the sparse Fourier transform: A compressed Fourier transform for big data, *IEEE Signal Processing Magazine* **31**, 91 (2014).
- [87] J. Preskill, Quantum Computing in the NISQ era and beyond, *Quantum* **2**, 79 (2018), [arXiv:1801.00862](https://arxiv.org/abs/1801.00862) [quant-ph].
- [88] S.-J. Ran, Encoding of matrix product states into quantum circuits of one- and two-qubit gates, *Physical Review A* **101**, 032310 (2020), [arXiv:1908.07958](https://arxiv.org/abs/1908.07958) [quant-ph].
- [89] Z.-Y. Wei, D. Malz, and J. I. Cirac, Sequential generation of projected entangled-pair states, *Physical Review Letters* **128**, 010607 (2022), [arXiv:2107.05873](https://arxiv.org/abs/2107.05873) [quant-ph].
- [90] M. P. Zaletel and F. Pollmann, Isometric tensor network states in two dimensions, *Physical Review Letters* **124**, 037201 (2020), [arXiv:1902.05100](https://arxiv.org/abs/1902.05100) [cond-mat.str-el].
- [91] G. Vidal, Class of quantum many-body states that can be efficiently simulated, *Physical Review Letters* **101**, 110501 (2008), [arXiv:quant-ph/0610099](https://arxiv.org/abs/quant-ph/0610099) [quant-ph].
- [92] T. P. Krasulina, The method of stochastic approximation for the determination of the least eigenvalue of a symmetrical matrix, *USSR Computational Mathematics and Mathematical Physics* **9**, 189 (1969).
- [93] O. Shamir, A stochastic PCA and SVD algorithm with an exponential convergence rate, in *Proceedings of the 32nd International Conference on Machine Learning*, Proceedings of Machine Learning Research, Vol. 37, edited by F. Bach and D. Blei (PMLR, Lille, France, 2015) pp. 144–152, [arXiv:1409.2848](https://arxiv.org/abs/1409.2848) [cs.LG].
- [94] O. Shamir, Fast stochastic algorithms for SVD and PCA: Convergence properties and convexity, in *Proceedings of The 33rd International Conference on Machine Learning*, Proceedings of Machine Learning Research, Vol. 48, edited by M. F. Balcan and K. Q. Weinberger (PMLR, New York, New York, USA, 2016) pp. 248–256, [arXiv:1507.08788](https://arxiv.org/abs/1507.08788) [cs.LG].
- [95] D. V. Savostyanov and I. Oseledets, Fast adaptive interpolation of multi-dimensional arrays in tensor train format, in *The 2011 International Workshop on Multi-dimensional (nD) Systems* (2011) pp. 1–8.
- [96] D. V. Savostyanov, Quasioptimality of maximum-volume cross interpolation of tensors, *Linear Algebra and its Applications* **458**, 217 (2014), [arXiv:1305.1818](https://arxiv.org/abs/1305.1818) [math.NA].
- [97] S. Dolgov and D. V. Savostyanov, Parallel cross interpolation for high-precision calculation of high-dimensional integrals, *Computer Physics Communications* **246**, 106869 (2020), [arXiv:1903.11554](https://arxiv.org/abs/1903.11554) [math.NA].
- [98] E. M. Stoudenmire and D. J. Schwab, Supervised learning with quantum-inspired tensor networks, in *Advances in Neural Information Processing Systems*, Vol. 29, edited by D. Lee, M. Sugiyama, U. Luxburg, I. Guyon, and R. Garnett (Curran Associates, Inc., 2016) pp. 4799–4807, [arXiv:1605.05775](https://arxiv.org/abs/1605.05775) [stat.ML].
- [99] J. A. Bengua, P. N. Ho, H. D. Tuan, and M. N. Do, Matrix product state for higher-order tensor compression and classification, *IEEE Transactions on Signal Processing* **65**, 4019 (2017), [arXiv:1609.04541](https://arxiv.org/abs/1609.04541) [stat.ML].
- [100] W. Huggins, P. Patil, B. Mitchell, K. B. Whaley, and E. M. Stoudenmire, Towards quantum machine learning with tensor networks, *Quantum Science and Technology* **4**, 024001 (2019), [arXiv:1803.11537](https://arxiv.org/abs/1803.11537) [quant-ph].
- [101] S. Efthymiou, J. Hidary, and S. Leichenauer, Tensor-Network for machine learning, *CoRR abs/1906.06329* (2019), [arXiv:1906.06329](https://arxiv.org/abs/1906.06329) [cs.LG].
- [102] E. Grant, M. Benedetti, S. Cao, A. Hallam, J. Lockhart, V. Stojevic, A. G. Green, and S. Severini, Hierarchical quantum classifiers, *npj Quantum Information* **4** (2018), [arXiv:1804.03680](https://arxiv.org/abs/1804.03680) [quant-ph].
- [103] J. R. McClean, S. Boixo, V. N. Smelyanskiy, R. Babush, and H. Neven, Barren plateaus in quantum neural network training landscapes, *Nature Communications* **9** (2018), [arXiv:1803.11173](https://arxiv.org/abs/1803.11173) [quant-ph].

- [104] A. Pesah, M. Cerezo, S. Wang, T. Volkoff, A. T. Sornborger, and P. J. Coles, Absence of barren plateaus in quantum convolutional neural networks, *Physical Review X* **11** (2021), [arXiv:2011.02966](https://arxiv.org/abs/2011.02966) [quant-ph].
- [105] E. C. Martín, K. Plekhanov, and M. Lubasch, Barren plateaus in quantum tensor network optimization, *Quantum* **7**, 974 (2023), [arXiv:2209.00292](https://arxiv.org/abs/2209.00292) [quant-ph].
- [106] H.-K. Zhang, S. Liu, and S.-X. Zhang, Absence of barren plateaus in finite local-depth circuits with long-range entanglement, arXiv preprint (2023), [arXiv:2311.01393](https://arxiv.org/abs/2311.01393) [quant-ph].
- [107] I. A. Luchnikov, A. Ryzhov, S. N. Filippov, and H. Ouerdane, QGOpt: Riemannian optimization for quantum technologies, *SciPost Physics* **10**, 79 (2021), Code available from <https://github.com/LuchnikovI/QGOpt>, [arXiv:2011.01894](https://arxiv.org/abs/2011.01894) [quant-ph].
- [108] I. A. Luchnikov, M. E. Krechetov, and S. N. Filippov, Riemannian geometry and automatic differentiation for optimization problems of quantum physics and quantum technologies, *New Journal of Physics* **23**, 073006 (2021), [arXiv:2007.01287](https://arxiv.org/abs/2007.01287) [quant-ph].
- [109] A. Oza, A. Pechen, J. Dominy, V. Beltrani, K. Moore, and H. Rabitz, Optimization search effort over the control landscapes for open quantum systems with Kraus-map evolution, *Journal of Physics A: Mathematical and Theoretical* **42**, 205305 (2009), [arXiv:0905.1149](https://arxiv.org/abs/0905.1149) [quant-ph].
- [110] M. Abadi, A. Agarwal, P. Barham, E. Brevdo, Z. Chen, C. Citro, G. S. Corrado, A. Davis, J. Dean, M. Devin, S. Ghemawat, I. Goodfellow, A. Harp, G. Irving, M. Isard, Y. Jia, R. Jozefowicz, L. Kaiser, M. Kudlur, J. Levenberg, D. Mané, R. Monga, S. Moore, D. Murray, C. Olah, M. Schuster, J. Shlens, B. Steiner, I. Sutskever, K. Talwar, P. Tucker, V. Vanhoucke, V. Vasudevan, F. Viégas, O. Vinyals, P. Warden, M. Wattenberg, M. Wicke, Y. Yu, and X. Zheng, *TensorFlow: Large-scale machine learning on heterogeneous systems* (2015), Code available from <https://www.tensorflow.org>, [arXiv:1603.04467](https://arxiv.org/abs/1603.04467) [cs.DC].
- [111] B. Jobst, K. Shen, C. A. Riofrio, E. Shishenina, and F. Pollmann, *Efficient MPS representations and quantum circuits from the Fourier modes of classical image data* (2023), Data analysis and simulation codes on Zenodo.
- [112] NIST Digital Library of Mathematical Functions (DLMF): Hurwitz zeta function (2022), <https://dlmf.nist.gov/25.11>. Release 1.1.8 of 2022-12-15. Frank W. J. Olver, Adri B. Olde Daalhuis, Daniel W. Lozier, Barry I. Schneider, Ronald F. Boisvert, Charles W. Clark, Bruce R. Miller, Bonita V. Saunders, Howard S. Cohl and Marjorie A. McClain, eds.